THESIS FOR THE DEGREE OF DOCTOR OF PHILOSOPHY

Sintering simulation framework for 316L stainless steel components manufactured by binder jetting

ALBERTO CABO RIOS

Department of Industrial and Materials Science
CHALMERS UNIVERSITY OF TECHNOLOGY
Gothenburg, Sweden, 2024

Sintering simulation framework for 316L stainless steel components manufactured by binder jetting

ALBERTO CABO RIOS

ISBN 978-91-8103-028-0

Doktorsavhandlingar vid Chalmers tekniska högskola

Ny serie nr 5486

ISSN 0346-718X

Department of Industrial and Materials Science

Chalmers University of Technology

SE-412 96 Gothenburg

Sweden

Telephone + 46 (0)31-772 1000

Printed by Chalmers digitaltryck

Gothenburg, Sweden 2024

Sintering simulation framework for 316L stainless steel components manufactured by binder jetting

Alberto Cabo Rios
Department of Industrial and Materials Science
Chalmers University of Technology

ABSTRACT

Binder Jetting (BJT) is an additive manufacturing (AM) technology allowing mass-production of small to medium-size metal components. BJT is a multi-step AM technology, where the geometrical shape of components is provided during the printing step, and the final properties are achieved through a second consolidation step - sintering. The sintered properties are achieved through densification of the porous (~40-60%) BJT parts, resulting in large volumetric shrinkages during the process. Furthermore, shape distortions are common due to sintering at high temperatures, close to the melting point of the metallic powder.

The first part of the thesis focusses on establishing an experimental characterization procedure for the sintering of BJT parts. The dimensional evolution from dilatometry experiments reveals the anisotropic sintering shrinkages with larger shrinkages along the building direction. Debinding does not induce substantial shrinkages (< 0.5%) or shrinkage anisotropy. Density fluctuations along the building direction related to the printing layer thickness of 42 μm were revealed, which decrease during sintering. An increase in shrinkage rate above ~1310°C was observed, related to the formation of δ-ferrite phase detected in samples sintered at 1370 °C.

The second part of the thesis focusses on the development and implementation of a phenomenological model of sintering based on experimental input from the first part. The model is based on the continuum theory of sintering and describes the particularities of the 316L stainless steel BJT components during sintering. The bulk viscosity dependency on porosity is studied by using different expressions with and without fitting constants. Also, a new material shear viscosity expression is proposed, which explicitly accounts for the effect of δ-ferrite formation on the sintering behavior.

The last part comprises the implementation of the model expressions in a commercial FEA software and the sintering simulation of BJT geometries that showcases predictions with less than ~1 mm deviation on the shape distortions due to gravity. Demonstrator components were designed, including overhang structures that lead to large shape deformations. Different sintering models' results are compared, where the ROH (Rios-Olevsky-Hryha) sintering model shows the best performance revealing small deviations of ~0.56 mm related to the isotropic assumption of the model.

This works paves the ground for its expansion to component manufactured using different BJT printers and stainless steel powders. Moreover, it has a high application potential to other sinter-based manufacturing technologies.

Keywords: Sintering, binder jetting, dilatometry, additive manufacturing, sintering modelling, stainless steel.

PREFACE

This doctoral thesis is based on the work performed at the Department of Industrial and Materials Science at Chalmers University of Technology from April 2019 to February 2024, and in the Powder Technology Laboratory at San Diego State University (SDSU) from August 2021 to December 2022. The work has been carried out under the supervision of Professor Eduard Hryha (Chalmers), Professor Eugene Olevsky (SDSU) and Professor Lars Nyborg as examiner. This work has been performed within the framework of Centre for Additive Manufacture-Metal (CAM^2), as a PhD project financed by Sandvik AB (during the first years), Digital Metal AB and Höganäs AB.

List of appended papers

Paper I: **Sintering anisotropy of binder jetted 316L stainless steel: part I – sintering anisotropy.**
Alberto Cabo Rios, Eduard Hryha, Eugene Olevsky, Peter Harlin.
Powder Metallurgy, Vol. 65(4), 2022, 273-282.
DOI: https://doi.org/10.1080/00325899.2021.2020485

Paper II: **Sintering anisotropy of binder jetted 316L stainless steel: part II – microstructure evolution during sintering.**
Alberto Cabo Rios, Eduard Hryha, Eugene Olevsky, Peter Harlin.
Powder Metallurgy, Vol. 65(4), 2022, 283-295.
DOI: https://doi.org/10.1080/00325899.2021.2020486

Paper III: **Analytical models for initial and intermediate stages of sintering of additively manufactured stainless steel.**
Alberto Cabo Rios, Eugene A. Olevsky, Eduard Hryha, Mats Persson, Rajendra K. Bordia.
Acta Materialia, Vol. 249, 2023, 118822.
DOI: https://doi.org/10.1016/j.actamat.2023.118822

Paper IV: **Modelling of δ-ferrite transformation effect on the sintering behaviour of 316L binder jetted components.**
Alberto Cabo Rios, Eugene A. Olevsky, Eduard Hryha, Mats Persson.
WorldPM2022 Conference proceedings, 2022.

Paper V: **Ex-situ characterization and simulation of density fluctuations evolution during sintering of binder jetted 316L.**
Alberto Cabo Rios, Tatiana Mishurova, Laura Cordova, Mats Persson, Giovanni Bruno, Eugene Olevsky, Eduard Hryha.
Materials & Design, Vol. 238, 2024, 112690.
DOI: https://doi.org/10.1016/j.matdes.2024.112690

Paper VI: **Sintering Simulation and Experimental Validation of 316L Pipe Tee Connectors Printed by Binder Jetting Additive Manufacturing.**
Elisa Torresani, Alberto Cabo Rios, Thomas Grippi, Andrii L. Maximenko, Marco Zago, Ilaria Cristofolini, Eugene A. Olevsky.
Manuscript.

Paper VII: **Modelling of gravity-affected sintering of additively manufactured stainless steel components.**
Alberto Cabo Rios, Mats Persson, Eduard Hryha, Eugene A. Olevsky.
Manuscript (submitted).

Contribution to the appended papers

Paper I: The author planned the study in collaboration with the co-authors. The author performed all the experimental work, except the printing that was performed at Sandvik. The author analyzed the data and wrote the paper in collaboration with the co-authors.

Paper II: The author planned the study in collaboration with the co-authors. The author performed all the experimental work, except the printing and chemical analysis that was conducted at Sandvik. The author analyzed the data and wrote the paper in collaboration with the co-authors.

Paper III: The author planned the study in collaboration with the co-authors. The author performed all the experimental work, the samples printing that was done at Digital Metal. Analysis of results and writing of the manuscript was performed in collaboration with the co-authors.

Paper IV: The author planned and performed all the experimental work, the samples printing that was done at Digital Metal. Analysis of results was performed in collaboration with the co-authors. The author wrote the paper with the help of co-authors.

Paper V: This study was planned together with the coauthors. The samples were printed and pre-sintered by M. Persson at Digital Metal. XCT experiments were conducted by Tatiana Mishurova at BAMline, Germany. The analysis of the data and simulations were conducted by the author. The author wrote the paper with the help of co-authors.

Paper VI: This study was planned by the author E. Torresani together with the co-authors. The experimental work (components printing and measurements) was done by M. Zago and I. Cristofolini and the simulations were conducted by A. Cabo Rios. The analysis of the data and the manuscript writing was done in collaboration with the author and co-authors.

Paper VII: The author planned and performed most of the experimental work together with the co-authors. The components printing and sintering was done at Digital Metal. The X-Ray CT characterization was performed by Nikon Metrology Europe. The simulations and analysis of results was performed in collaboration with the co-authors. The author wrote the paper with the help of co-authors.

Table of Contents

Nomenclature

θ	Porosity
V_P	Pore volume
V_T	Total volume
ρ	Density
$\dot{\theta}$	Porosity elimination rate (s^{-1})
$\dot{e}$	Trace of the strain rate tensor (s^{-1})
$\dot{\boldsymbol{\varepsilon}}_{ij}$	Strain rate tensor (s^{-1})
$\dot{\boldsymbol{\varepsilon}}_{ij}^{in}$	Inelastic strain rate tensor (s^{-1})
$\boldsymbol{\sigma}_{ij}$	Stress tensor ($N \cdot m^{-2}$)
$\boldsymbol{\sigma}'_{ij}$	Deviatoric component of stress tensor ($N \cdot m^{-2}$)
σ_m	Hydrostatic component of stress tensor ($N \cdot m^{-2}$)
P_L	Effective sintering stress (Pa)
K	Effective bulk modulus
G	Effective shear modulus
φ	Normalized shear modulus
ψ	Normalized bulk modulus
δ_{ij}	Delta de Kronecker
η_0	Material viscosity ($Pa \cdot s$)
A_0	Viscosity pre-exponential factor ($Pa \cdot s \cdot K^{-1}$)
Q	Viscosity activation energy ($J \cdot mol^{-1}$)
R	Gas constant = 8.314 ($J \cdot mol^{-1} \cdot K^{-1}$)
T	Temperature (K)
α	Surface energy ($J \cdot m^{-2}$)
r_0	Initial particle mean radius (m)
t	Time (t)
$\dot{G}$	Grain growth rate ($m \cdot s^{-1}$)
G	Grain size diameter (m)
k_0	Grain growth pre-exponential factor ($\mu m^3 \cdot s^{-1}$)
Q_{G}	Grain growth activation energy ($J \cdot mol^{-1}$)
ρ_c	Grain growth critical density
θ_c	Normalized bulk viscosity constant (critical porosity)
A	Normalized bulk viscosity constant
B	Normalized bulk viscosity constant
A_1	Piece-wise viscosity pre-exponential factor below T_T ($Pa \cdot s \cdot K^{-1}$)

Q_1	Piece-wise viscosity pre-exponential factor above T_T $(Pa \cdot s \cdot K^{-1})$
T_T	Transition temperature (K)
A_2	Piece-wise activation energy below T_T $(J \cdot mol^{-1})$
Q_2	Piece-wise activation energy above T_T $(J \cdot mol^{-1})$
A_γ	Pre-exponential viscosity factor of γ
A_δ	Pre-exponential viscosity factor of δ
Q_γ	Activation energy of γ
Q_δ	Activation energy of δ
ρ_{Geom}	Relative density calculated by volume and mass measurements
ρ_{Arch}	Relative density calculated by Archimedes method
ρ_{LOM}	Relative density calculated from Light Optical Microscopy image analysis

CHAPTER 1: INTRODUCTION

1.1 Background & motivation

Additive manufacturing (AM) is defined as a "process of joining materials to make objects from 3D model data, usually layer upon layer, as opposed to subtractive manufacturing methodologies" [1]. AM offers some unique advantages such as minimizing material waste, reducing manufacturing chain and minimizing delivery times, and manufacturing highly complex geometries [2–6]. While most metal AM technologies are not widely used for mass production due to low productivity and high costs, Binder Jetting (BJT) is emerging as an AM technology with promising potential for low-cost mass production across various industries (e.g., structural applications, automotive, consumer products, biomedical, aerospace, etc.). However, several challenges must be addressed to unlock the full potential of this technology.

Metal Binder Jetting is classified as a multi-step AM process, where the first step provides the basic geometric shape (printing), and the following steps consolidates the part to the intended basic material properties (sintering) [1]. The accuracy and resolution of the BJT printing process is intrinsically high because of the small size of the binder droplets and powder used. Moreover, there has been a continuous development of advanced industrial BJT systems during the last decades. However, considering the challenge of predicting geometrical distortion during the sintering step, the final accuracy of binder jetting manufacturing may be drastically reduced [7]. Consequently, one of the main challenges for the BJT technology is not directly related to the printing process but with the sintering step. The as-printed components are characterized by high porosity (40-60%) and their dimensions may shrink up to ~25% during the sintering process when reaching full densification. Additionally, large geometrical distortions may occur due to the high sintering temperatures required and the influence of external forces (e.g. gravity, friction, etc.).

All the geometrical changes occurring during sintering must be compensated during the component design process to achieve a sintered geometry that fulfills the required tolerances. Traditionally, manufacturers have relied on the trial-and-error experimental process and manual design modifications. However, this methodology typically requires a high degree of expertise and several iterations, leading to significantly longer times and higher costs in order to achieve the required final components. The use of simulation tools has the potential to solve most of the challenges related to the geometrical changes during the sintering process. Sintering models have been traditionally developed focusing on other powder metallurgy (PM)

technologies like press and sintering or spark plasma sintering [8–20]. But very few studies have been focused on the modelling of sintering of metal BJT components [21–25]. Recently, sintering simulation tools like Live Sinter (Desktop Metal) or Simufact additive (Hexagon) has been introduced on the AM market. However, there is a need for a general simulation framework that can be implemented and used for a wide combination of the BJT systems and metal powders available on the market. Moreover, the research and development of sintering models serves to foster the knowledge and understanding of the BJT sintering process and opens new opportunities for its optimization.

1.2 Objectives

By investigating the sintering behavior of BJT parts, this thesis seeks to identify and develop critical parameters for a comprehensive phenomenological model of the sintering process, ultimately contributing to the optimization and control of BJT additive manufacturing. The experimental investigation of the sintering process was done to understand the impact of the characteristics of the BJT parts during the sintering process and determine the necessary input for robust simulation framework. A phenomenological model of sintering was proposed together with the methodology for the identification of the material constants and required material and experimental input. Ultimately, the model was implemented and solved by Finite Element Method (FEM) and validated against experimental data from the characterization of complex BJT components.

Consequently, the following research questions (RQ) are formulated from these objectives:

RQ1: What is the impact of the characteristics of green BJT components and sintering process on densification shrinkages during the sintering?

RQ2: How does the microstructural evolution during sintering affects the sintering behavior of BJT stainless steel components?

RQ3: What are the main material parameters required for a comprehensive sintering model, and how can they be identified experimentally for binder jetted stainless steel?

RQ4: What is the impact of model parameters and BJT geometries on dimensional accuracy and applicability of the developed phenomenological sintering model?

1.3 Research strategy

During the binder jetting additive manufacturing process, there are a handful of factors that affect the evolution of the components during the sintering process. From the properties of the powder and BJT printer system, to the execution variables of the debinding and sintering process. The first part of this thesis is focused on the detailed experimental study of the sintering process of BJT samples. The external dimensions and the microstructural characteristics were characterized throughout the sintering process until nearly full densification is reached. Two combinations of BJT printers and powders were used, but the development of the printing parameters is out of the scope of this thesis. Nevertheless, the impact of these different printers and powders on the green component and, consequently, on the sintering behavior was addressed to some extent. The second part of this thesis is focused on the development and validation of a simulation framework for the prediction of the sintering behavior of BJT 316L stainless steel components. For that purpose, commercially available COMSOL Multiphysics® simulation software was used for the implementation of the proposed model formulation using existing modules (e.g. solids mechanics module) and the post-processing of simulation results. The algorithms used for the processing and analysis of the experimental data were implemented using MATLAB® [26]. While new solid mechanics formulations are beyond the scope of this research, the methodology involved extensive adaptation and tailoring of existing models. Material properties, constitutive equations, and boundary conditions were meticulously chosen and adjusted to represent the unique characteristics of the sintering process and BJT materials.

In summary, the first research questions are related to the experimental characterization of the BJT printed components, density and microstructure evolution during the sintering process, and characterization of the sintered components (RQ1 and RQ2). Based on the knowledge gathered from experimental data, a phenomenological sintering model was proposed together with the methodology for the identification of the required material constants (RQ3). Ultimately, Finite Element Method (FEM) simulations were done for various cases with relevant geometries to validate and evaluate the simulation performance (RQ3 and RQ4).

Due to the collaborative nature of this applied project and the resources allocation, different combinations of powder materials and BJT printers of interest were used for the manufacturing of the components. Table 1 summarizes the data regarding the used powder material and BJT system, along with the indication of what RQ was mainly addressed within the corresponding paper.

Table 1. List of the powders and BJT systems used in each paper, along with the focus of the study in relation to the specific RQs.

Paper	RQ1	RQ2	RQ3	RQ4	Powder	BJT system
Paper I					Sandvik Osprey® 316L	ExOne Innovent+
Paper II						
Paper III					DM 316L	Digital Metal DM P2500 (P1710 in Paper VI)
Paper IV						
Paper V						
Paper VI						
Paper VII						

CHAPTER 2: BINDER JETTING METAL ADDITIVE MANUFACTURING

Binder Jetting (BJT) is a versatile additive manufacturing (AM) process that can be applied to various powdered materials, including polymers, metals, and ceramics. Currently, powder bed fusion – laser beam of metals (PBF-LB/M) is the most widespread AM technology when it comes to metals. However, binder jetting offers several advantages that make this technology able to overcome the limitations for the mass production of complex components. BJT can achieve faster production rates, eliminates the need for support structures, and enables component stacking for maximum build volume utilization, substantially reducing the part cost [27]. This makes BJT a promising alternative for cost-effective mass production of AM metal components.

Binder Jetting is classified as a multi-step additive manufacturing (AM) process [1], where the first operation provides the basic part geometrical shape (BJT printing) and the following consolidates the part to reach final geometry and intended basic material properties (sintering). The typical metal BJT additive manufacturing process encompasses the following main stages: printing, curing, depowdering, debinding, and sintering, as illustrated in Figure 1. After BJT printing, the build box is heated inside an oven for binder curing, which strengthens the printed components. Subsequently, the green parts are removed from the build-box during depowdering. Finally, the parts undergo debinding, followed by sintering in a high-temperature furnace to consolidate them. The characteristics of the main steps (i.e. printing, debinding and sintering) are detailed in the next sections.

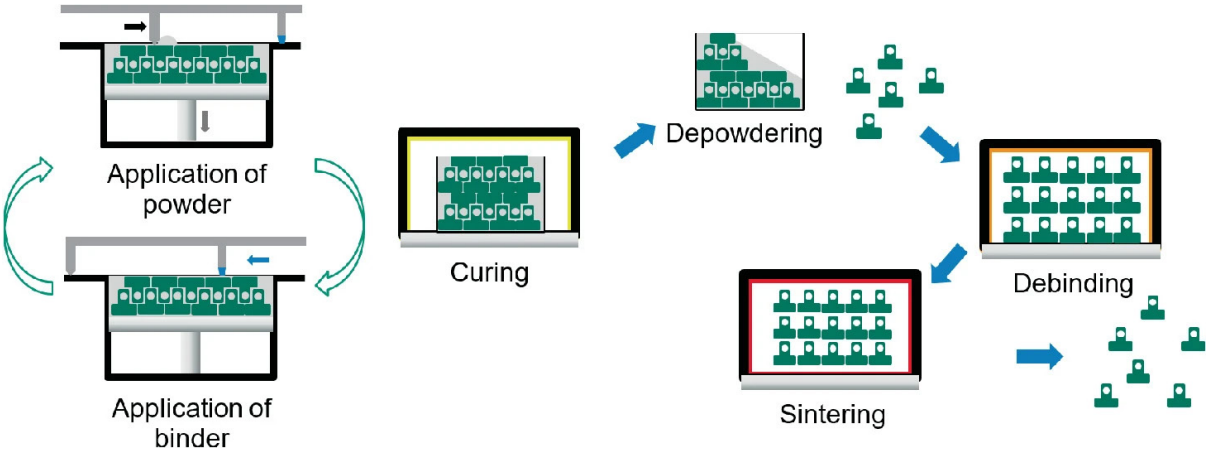

Figure 1. Metal binder jetting process chain [27].
Reproduced with permission from Springer Nature.

2.1 Binder Jetting Printing

The binder jetting printing process begins by evenly spreading a layer of powder material within a build-box. Then, a printhead selectively deposits liquid binder in specific areas on top of the powder layer, forming a network of interconnected powder particles. This process is repeated layer by layer, gradually building up the desired three-dimensional geometry within the powder bed. Typically, BJT printers can be divided into several main parts, including the binder deposition system, powder dispensing and recoating system, build platform and excess powder collecting chamber (illustrated in Figure 2). However, a diverse range of binder jetting printer systems exists, each employing distinct configurations and capabilities. These variations usually stem from differences in powder bed size, printhead architecture, powder dispensing and recoating approaches, etc.

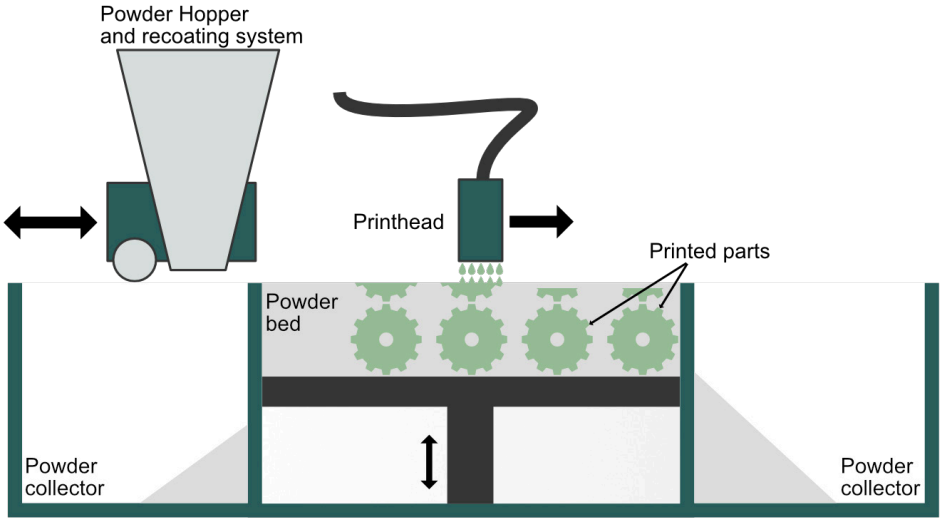

Figure 2. Schematic illustration of the BJT printing process.

In general, the main sub-systems affecting the as-printed (green) part characteristics are the binder deposition system and the powder deposition system. These two systems move over the powder bed to complete the necessary steps of the printing process. Typically, this movement is linear and is produced along different directions for each sub-system. At the same time, the operation of these systems is governed by adjustable parameters that control the printing process, affecting the properties of the green (as-printed) parts and, thus, the sintered components. The operation of these systems, together with the characteristics of the powder feedstock used, are the main factors that determine the powder particles arrangement within the BJT green parts, as summarized in Figure 3.

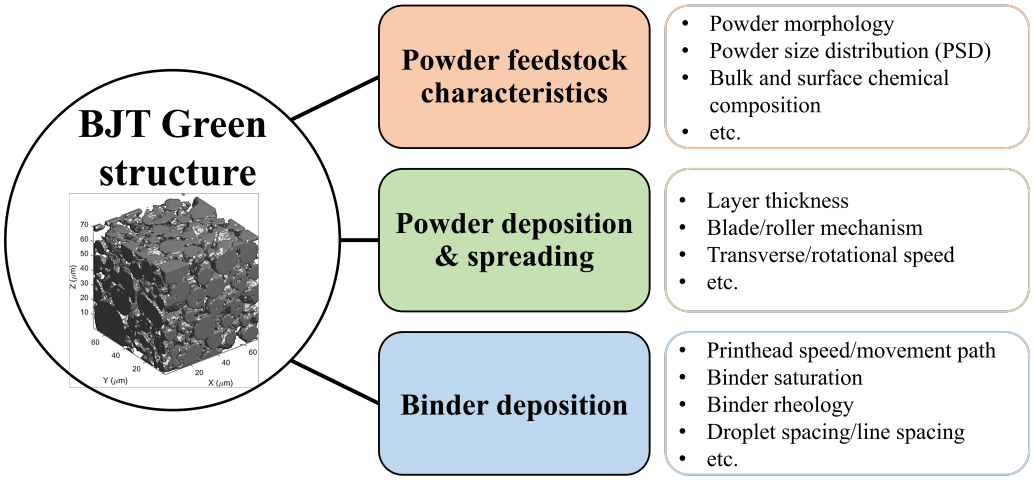

Figure 3. Main factors that determine the characteristics of the BJT green components.

2.1.1 Powder feedstock properties

The powder feedstock used in Binder Jetting Technology (BJT) is characterized by several properties, including particle morphology, particle size distribution (PSD), and bulk/surface chemical composition. Powder size and morphology play a crucial role in determining the printability of the material. Typically, spherical powders are used in powder-based additive manufacturing processes because of the good flowability properties [7,21,28]. However, the production methods required for these powders (gas atomization) increase its cost when compared to irregular shaped powder produced by water atomization. Particle size distribution (PSD) is a crucial factor in Binder Jetting Technology (BJT) as it directly affects the printing, and ultimately the sintering behavior of the material [29–32]. The atomization process typically produces normal (Gaussian) PSD distribution, which can be characterized by cumulative percentile values such as D10, D50, and D90. The particle size of BJT powders can vary widely, ranging from hundreds of nanometers to ~30 μm. Smaller particles (<5 μm) exhibit enhanced sintering activity, leading to faster densification. However, they also tend to agglomerate during the printing process, hindering printing quality. In contrast, larger particles (>5 μm) offer improved flowability and higher packing density, facilitating printing but resulting in lower densification. Therefore, the PSD of the powders used has a crucial influence during the entire BJT manufacturing.

All these powder characteristics have a decisive effect on the inherent packing density. Apparent density describes the loose, undisturbed state of the powder, while tap density is the density of the powder in a container that has been tapped under specified conditions [33,34]. The BJT printing process induces packing densities on the powder bed between the apparent and tap density. Consequently, green relative densities of the BJT components typically range between 40-60%. This powder

packing is essential for the later debinding and sintering steps of the manufacturing process.

2.1.2 Powder deposition

The main function of the powder deposition system is to deposit a uniform layer of powder on top of the powder bed. Depending on the printer, this system may work using different mechanisms for the powder deposition and spreading. The arrangement of the particles within the powder bed is, therefore, determined by the interactions of the powder material with this system. This process can be divided into two steps: powder deposition and spreading. Deposition is the method used to place the powder on top of the build box and is typically divided into piston-based and hopper feeder systems. Spreading is done when the powder deposited needs to be uniformly distributed to create a uniform layer. Spreading systems are typically based on recoating blades or rollers with transverse and rotational movement [35]. For instance, one of the BJT printers used in this work (ExOne Innovet +) employs an ultrasonic hopper dispensing system, followed by a rotating roller that spreads the powder [36]. Previous research studied in detail the influence of these different mechanisms on the packing density distribution of the powder bed [21,35,37–40]. For instance, in [21] the results suggested that roller recoating systems may induce the segregation of finer powder particles at the bottom of the deposited layer. The powder deposition systems can be tuned by several operating parameters (e.g. ultrasonic intensity, roller traverse and rotational speed) that will determine particle's arrangement within the layer after the spreading step.

2.1.3 Binder deposition

The system responsible for depositing binder onto the powder bed comprises various components, the most crucial of which are the printhead, the printhead movement mechanism, and the binder solution. This system is specifically designed to move over the powder bed while selectively dropping the liquid binder on top of each previously deposited layer of powder. The powder-binder interaction has an influence on the final powder bed packing and porous structure of the BJT green components. Previous investigations have shown disturbances that the impact of binder droplets can induce on the powder bed [41,42]. Also, the flowing behavior of the deposited powder layers is affected by the restricted flowability of the previously bonded powder, potentially inducing a "layered" pore structure on the green part [43]. The binder deposition system is controlled as well by a set of printing parameters that can be tuned to reach the desired BJT part characteristics (e.g. binder saturation, droplet spacing, etc.). Therefore, the optimization of this process is crucial for the control of the BJT green

components and may affect its behavior during the sintering process. Finally, the liquid binder is also of great importance during the printing process to ensure geometrical precision and strength of the printed BJT components.

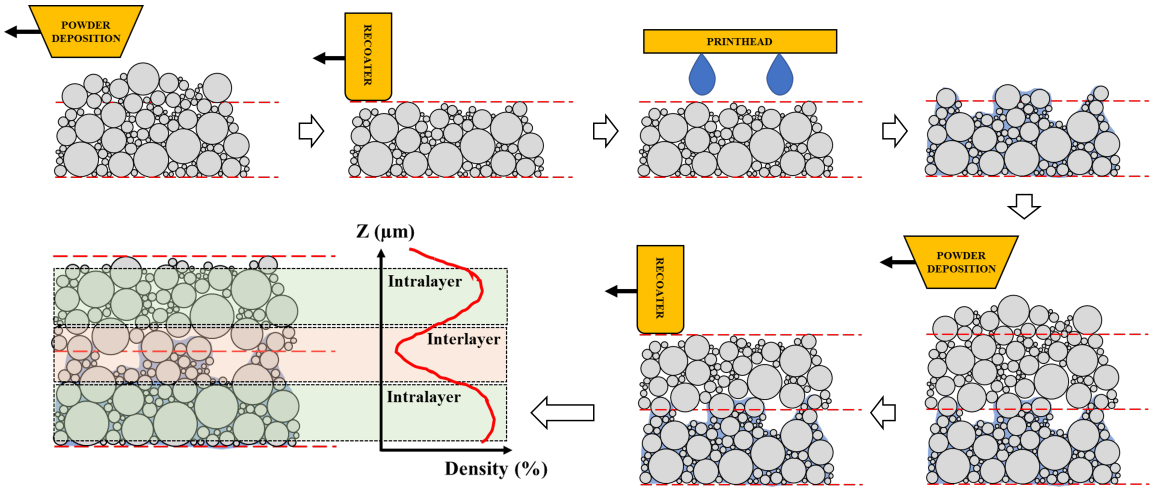

Figure 4. Illustration of the BJT printing process and its impact on the powder packing and density fluctuation along the building direction [44].

2.2 Debinding

Before sintering, effective removal of binder from within the "green" component is crucial. Through pyrolysis at low temperatures, the debinding process decomposes and evaporates the binder, usually in the same sintering cycle or beforehand. The typical use of polymers in the binders can lead to the presence of carbon residues after debinding [45,46], which could later diffuse into the alloy and influence the microstructure and phase transformations during sintering [22]. However, appropriate debinding process and sintering atmosphere can minimize these residues, making this effect negligible during the sintering process and final part properties. This influence mainly depends on the binder composition and powder material. Thermal analysis techniques like thermogravimetry analysis (TGA) are commonly used for precisely measuring binder removal, including decomposition and evaporation, and optimize the debinding process. However, in this thesis study, available commercial binders and manufacturer-recommended debinding processes are employed.

2.3 Sintering

Green (as-printed) BJT parts have minimal mechanical strength due to the large porosity and weak bonding provided by the binder, requiring further processing like sintering to reach the required material properties. Sintering can be defined as a thermal treatment that leads to particle bonding and further consolidation into a solid

structure via mas transport mechanisms. This densification process results in the strengthening of the components after sintering. Therefore, the sintering process in BJT manufacturing is a crucial step to achieve the desired final component. The BJT parts typically undergo severe changes during the sintering step: volumetric shrinkages, geometrical shape evolution and microstructure changes (e.g. pore structure and grain size).

Binder Jetting can be used for manufacturing a wide range of metallic components by employing metal powders such as steel alloys, titanium alloys, nickel-based superalloys, copper, etc. At the same time, every material is different from each other in terms of powder characteristics, thus, the printing process needs to be optimized. The printing process (through its influence on particle's arrangement within the BJT green part) and the alloy composition of the powder material significantly impact the sintering process. Consequently, it is crucial to understand the sintering behavior of each specific material and adjust the sintering process (e.g. time, temperature, and atmosphere) to reach the required properties of the sintered parts. In general, sintering can be classified depending on the presence of liquid phase during the process as:

- Solid-Sate Sintering (SSS) is driven by a combination of diffusion mechanisms (e.g. surface, grain boundary and volume diffusion), where atoms migrate across the porous material to bond particles and densify the green parts without liquid phase. This process is typically done for alloys where diffusion is high enough to achieve densification in a reasonable time.
- Liquid Phase Sintering (LPS) is driven by the adherence of solid particles promoted by liquid formation. Typically, this process is performed to sinter composite materials that employ different powder materials, in which one has a substantially lower melting temperature (binder phase) like hardmetals (WC-Co) or Fe-Cu alloys.
- Supersolidus Liquid Phase Sintering (SLPS) utilizes the melting behavior of metallic alloys. By heating the material to a temperature between its liquidus and solidus points, a fraction of liquid phase forms within the component, significantly enhancing densification. This effect can be precisely controlled by adjusting the sintering temperature within this specific temperature range [47].

Preferentially, BJT components are sintered by solid-state sintering to avoid potential shape deformations due to the presence of liquid phase [48,49]. Yet, some alloys (e.g. Nickel-based alloys like 718 [50] and 625 [51], and some low alloyed steels [52]) require some fraction of liquid phase to be densified in reasonable times because of the inherent low diffusion activity during solid-state sintering. The most common alloys for BJT manufacturing can reach high sintered relative densities of between

95 to 99.9% [2,28]. This thesis study has been focused on the solid-state sintering of stainless steel BJT parts, specifically the 316L alloy, which will be detailed in section 4.

2.4 Design for AM binder jetting (DfAM)

One of the biggest advantages of additive manufacturing in general, including binder jetting (BJT), is the excellent design flexibility. Yet, the design of BJT components has some particular challenges predominantly related to the risk of geometrical deformations occurring during the sintering process. A set of design guidelines and limitations have been established in parallel with the development of this technology [53]. However, these design limitations are one of the obstacles for the extensive implementation of this technology. In general, the geometrical changes during the sintering process can be roughly divided into two main categories: densification shrinkages and geometrical shape distortions.

Figure 5. Categorization of influences on component design in the metal binder jetting process chain [27]. *Reproduced with permission from Springer Nature.*

Densification shrinkages are linked to the overall decrease of the external dimensions caused by densification. These dimensional changes are typically compensated by scaling up the original design using factors derived from experimental test coupons subjected to the same sintering process. Note that the characteristic heterogeneous arrangement of particles within the BJT parts, typically requires the use of different scaling factors for each printing direction [53]. On the other hand, geometrical distortions occur during the sintering process due to the change in powder material properties with temperature and porosity of the BJT parts. Also, inhomogeneities within porous components can lead to shape distortions during sintering [54–57]. Generally, the external forces (e.g. gravity and friction) are the sources for these shape distortions during BJT sintering [58]. It is extremely difficult to avoid these distortions, but different approaches can be implemented to mitigate them. One typical method in industry is the manufacturing of support structures that shrink together with the component – such called "live setters", which are discarded afterwards. However, this method requires extensive expertise and trial-and-error for its correct implementation. Moreover, it comes with a significant waste of material and increased cost.

Predictive tools and compensation algorithms offer the most promising solution to compensate for geometrical changes during sintering of BJT parts. Early successes with analytical models for simple features like cylinders and holes [59,60] demonstrate its potential. However, the most exciting approach lies in combining macroscale finite element method (FEM) models of the sintering process with iterative geometry compensation algorithms [61]. In this approach, the CAD model is used for the sintering simulation which calculates the final sintered geometry. Then, a compensation algorithm creates a new pre-distorted geometry. This geometry is subjected again to the sintering simulation and the result is compared with the original CAD. This iterative process is repeated until the deviations between the calculated and CAD geometry are below the required tolerances. This powerful combination holds the key to unlocking the full design freedom potential of the binder jetting AM by accurately predicting and compensating for distortions.

CHAPTER 3: SINTERING OF STAINLESS STEEL

The main goal during the sintering of any powder metallurgy (PM) component is the promotion of particle bonding and further densification of the green components, in order to meet the required final properties after sintering. Therefore, the understanding and control of the material microstructure evolution as function of the powder characteristics and sintering treatment is essential. At the initial state, the system (gren part) has a high excess energy due to the relatively high specific surface area of the metal powders. The driving force behind metal powder sintering is the minimization of the system's total energy. Increasing the sintering temperature significantly accelerates this process, as higher thermal energy unlocks more efficient atomic diffusion mechanisms.

Figure 6 illustrates a comprehensive overview of various diffusion mechanisms operative during the solid-state sintering of metal powders. Each mechanism, including surface, grain boundary and volume diffusion, exhibits varying degrees of activity and influence on the microstructural changes that occur during the initial, intermediate, and final stages of sintering. Initially, activation of surface and grain boundary diffusion promotes formation of "necks" between particles without major densification, creating interconnected pores. During the intermediate stage, while these mechanisms remain present, higher temperatures enhance grain-boundary and bulk diffusion. This leads to significant densification, shrinkage, and isolation of the pores. During the final stage, the remaining pores are minimized and spheroidized for energy reduction, which also may lead to enhanced grain growth.

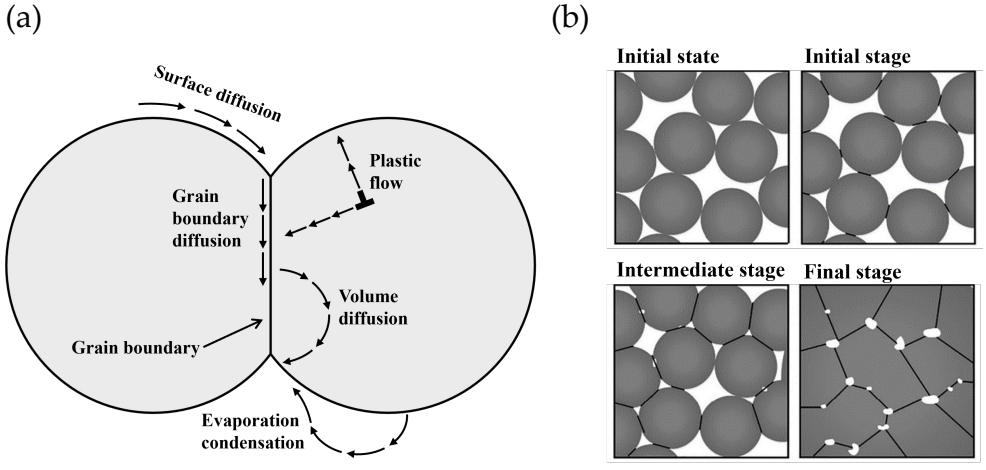

Figure 6. Illustration of the sintering mass transport mechanisms (a) and stages of the sintering process (b), redrawn from [62].

Apart from densification, metallic materials may undergo other microstructure changes during the solid-state sintering process such as grain growth and phase transformations. These transformations have a critical impact on the diffusion mechanisms, and ultimately on the sintering densification behavior of metal powders. Previous studies have shown that grain growth kinetics is influenced by the evolution of the pore morphology [62,63]. In the initial stage, the grain growth kinetics is low due to the pinning effect from the large open porosity. The pinning effect decreases as the pores become smaller and isolated. Then, the reduced porosity and increase in temperature leads to a significant rise of grain growth kinetics. However, grain boundaries act as high diffusion paths for densification, thus, the separation of grain boundaries from the pores has a negative impact on the densification rate. This behavior is initially influenced by the powder particle size and the porous structure of the BJT green parts. In conclusion, the degree of densification and microstructural evolution during sintering can be optimized by the selection of powder characteristics, printing parameters and sintering cycle. Sintering typically requires temperatures close to the melting temperature of the metal powder by heating in a conventional furnace at low to moderate heating rates. The metallic solid phase may undergo various phase transformations driven by the evolution of the thermodynamic equilibrium conditions, which would also impact the sintering behavior.

Sintering of stainless steels has been a common practice within various industries for decades. Several factors must be considered for the successful sintering of these materials. The high chromium (Cr) content of stainless steels leads to great corrosion resistance but brings challenges during sintering due to its strong affinity for nitrogen (N), carbon (C), and oxygen (O). So, the use of pure hydrogen atmosphere during sintering is usually preferred due to its ability to reduce oxides on the powder surface, ensuring densification and required final properties [64]. Another aspect that is highly dependent on the stainless steel alloy composition is the phase transformations that may occur during the sintering process. The main phases of these alloys are usually formed as FCC (γ-austenite) or BCC (α-ferrite and δ-ferrite) crystal structure. In general, the higher inherent diffusion of the BCC lattice enables a faster densification during sintering [45,64–66]. Particularly, for powder metallurgy components, the δ-ferrite phase transformation within the porous structure can boost the mass transport mechanism in different ways [66], as illustrated by Figure 7 (a). During the intermediate stage of sintering, mass transport mostly takes place along the γ grain boundary and γ lattice when microstructure is mainly austenitic. When δ-ferrite grains form along the γ grain boundaries, the mass transport pathways start changing. Then, mass transport occurs along the γ-δ grain boundaries and through the δ-ferrite grains (which has a higher bulk diffusivity) creating a "highway" for mass transport

between the pores that were connected to the previous γ grain boundaries. Consequently, the densification rate is boosted by this increase of the mass transport kinetics.

Some examples of this effect can be found in two of the most commercialized stainless steels for BJT manufacturing: 316L and 17-4 PH. These alloys typically undergo δ -ferrite (BCC) phase transformation within different temperature ranges depending on the alloy composition. For instance, 316L chemical composition may vary between 16% – 18% Cr and 10% - 14% Ni. The impact of this variation is illustrated by the phase diagram in Figure 7 (b), showing its large influence on the transition between the FCC (γ) → BCC (δ)+ FCC (γ) regions. Moreover, elements that are commonly found as interstitials within these metals (e.g. C and N) also impact the phase equilibrium by stabilizing the austenitic phase. Particularly, carbon (C) can affect the sintering behavior since it is one of the main elements of the binders used for BJT manufacturing. As shown in Figure 7 (c), carbon increases significantly the temperature for the formation of δ-ferrite while also decreasing the temperature for liquid formation. Yet, the use of appropriate debinding process together with reducing atmospheres (i.e. H_2) has been proven to be efficient to control increased interstitials (i.e. C and N) within the material [45,66,67]. In other cases, elements like boron can be intentionally added to enable faster densification at lower temperatures through the activation of supersolidus liquid phase sintering (SLPS) of the 316L powders [68]. In summary, this shows the crucial importance of the alloy composition of stainless steel during the sintering process. Moreover, the chemical composition can be further controlled for the optimization of the sintering process and final properties.

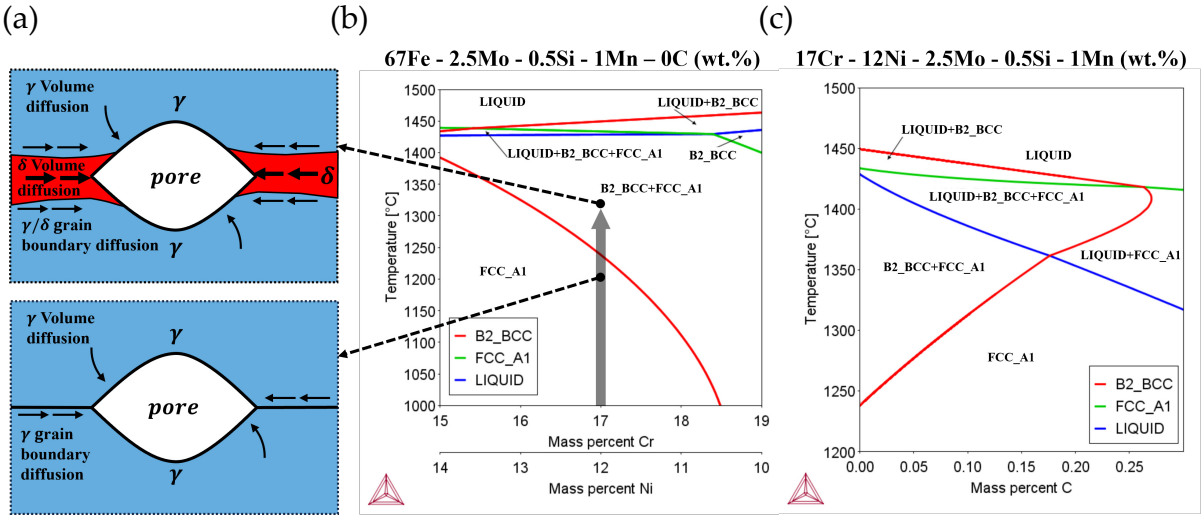

Figure 7. (a) Schematic diagrams of sintering mass transport difference between single phase γ and dual phase γ/δ microstructure. (b) Phase diagram showing effect of Cr-Ni variation on a phase composition of 316L alloy. (c) Phase diagram showing the effect of C content increase on phase composition.

CHAPTER 4: SINTERING MODELLING

Binder jetting aims for "net-shape" manufacturing, where both final geometry and properties are precisely controlled. This requires accurate modeling of the sintering process, as it significantly impacts both aspects through inevitable transformations of the printed metal components. Sintering modeling has evolved significantly over time, progressing from modeling the diffusion kinetic between particles to multi-scale modeling approaches [69–73]. While the initial models could predict individual particle interactions and time-dependent mass transport with high physical fidelity, their application is limited in practical engineering situations, where efficient macro-scale simulations are often necessary. Also, several macro-scale factors like the external forces (e.g. gravity and friction) and possible microstructural heterogeneities must be considered. Consequently, efforts have been mainly focused on the modelling of sintering at the macroscale level during the last decades with the aim of solving the practical problems of this technology [74–77]. The most popular approach is based on the use of continuum mechanics for the description of the powder particles compact as a continuum media. Several studies have been conducted analyzing different sintering processes and manufacturing techniques like Metal Injection Molding (MIM) [8,17], press and sintering [78], Spark Plasma Sintering (SPS) [10,14,16,18], and Microwave sintering [79–81]). However, very few recent studies have been focused on addressing the particularities of the sintering modelling of the BJT components [22–25].

The continuum modelling of sintering is the most relevant approach when calculating geometrical evolution, densification, and grain growth during sintering of complex geometries. Several sintering models and theories have been developed during the last decades [82–89]. Typically, these models are formulated using a constitutive formulation that relates the three-dimensional stress state of the material (stress tensor) to the strain rates (strain rate tensor) as for instance [90]:

$$\dot{\boldsymbol{\varepsilon}}_{ij}^{in} = \frac{\boldsymbol{\sigma}'_{ij}}{2G} + \frac{\sigma_m - P_L}{3K}\delta_{ij} \tag{1}$$

where $\dot{\boldsymbol{\varepsilon}}_{ij}^{in}$ is the inelastic shrinkage rate tensor; $\boldsymbol{\sigma}'_{ij}$ and σ_m are the deviatoric and volumetric parts of the stress tensor; G and K are the shear and bulk modulus of the continuum media; P_L is the effective sintering stress from the capillarity forces and δ_{ij} is the Kronecker delta function.

One of the main differences between these models relies on the determination of the material properties. Accordingly, these continuum models can be broadly classified

into phenomenological and physical models. In general, physical models intend to include explicitly the different diffusional mechanisms (i.e. grain boundary, surface, and volume diffusion, etc.) on the material parameters (i.e. shear and bulk modulus, and sintering stress) of the constitutive law at the various stages of sintering. For example, Riedel's model [84] is a comprehensive model that includes the different diffusion mechanisms that promotes sintering at different stages. However, these models require a vast number of material constants for their implementation (e.g. several diffusion coefficients or the grain boundary thickness) which are difficult to obtain experimentally. Also, these models include parameters which are typically obtained from fitting experimental data (e.g. normalized bulk viscosity).

At the expense of the detailed microscopic mechanisms, phenomenological models leverage the concept of a continuous, viscous porous medium to model high-temperature sintering. Some of the most used phenomenological models of sintering were developed by Olevsky et. al [88], Abouaf et. al [91,92], Hsueh et. al [93] and Bordia et. al [83,94]. These models vary depending on the intended process application from pressure assisted to pressure-less sintering process, and the material parameters expressions. The theory of sintering developed by Olevsky [88], due to its comprehensive formulation and versatility, was used as a basis to expand the modelling to the particularities of the sintering of BJT components treated in this thesis study. In this model, the BJT porous part is treated as a continuum porous medium consisting of a solid and porous volume fraction. During the sintering process, the evolution of these phases is represented by the relative density/porosity with the following relationship:

$$\theta = V_P/V_T = 1 - \rho \tag{2}$$

where V_T is the total volume; V_P the pore volume; ρ and θ the relative density and porosity.

The phenomenological model is constructed based on the assumption that the solid skeleton is composed of powder particles with the pores homogeneously distributed within the porous body. The skeleton is typically assumed to have a linear-viscous incompressible isotropic behavior during pressure-less sintering process, following the constitutive equation [88]:

$$\boldsymbol{\sigma}_{ij} = 2\eta_0 \left[\varphi \dot{\boldsymbol{\varepsilon}}'_{ij} + \left(\psi - \frac{1}{3}\varphi\right)\dot{e}\delta_{ij}\right] + P_L\delta_{ij} \tag{3}$$

where η_0 is the shear viscosity of the skeleton material (powder); φ and ψ are the normalized shear and bulk viscosity; P_L is the effective sintering stress and $\dot{e}$ is the volumetric strain rate.

The different terms of the constitutive equation (3) symbolize the different contributions to the material behavior: the left term $\boldsymbol{\sigma}_{ij}$ correspond to stresses from the external forces, the right term $P_L\delta_{ij}$ relates to the effective sintering stress (sintering driving force) and the middle term determines the resistance of the porous material to volumetric and shape deformations. The material behavior is then determined by the different parameters within the right part of the equation. The normalized viscosities (φ and ψ) derived from the rheological concepts of Skorohod [88,95], result in the following expressions of porosity:

$$\varphi = (1-\theta)^2 \tag{4}$$

$$\psi = \frac{2}{3}\frac{(1-\theta)^3}{\theta} \tag{5}$$

However, these expressions stem from theoretical assumptions of a complex porous structure. This generalization becomes less accurate as porosity increases, which may be significant in green Binder Jetting (BJT) components with high porosity levels. As illustrated in Figure 8, among various other models proposed in the literature, the normalized bulk modulus can have different expressions depending on the model proposed. Although a universal sintering model remains elusive, previous and ongoing research across various materials and sintering processes lays the foundation for its eventual development.

Du & Cocks 2nd stage	Ponte castaneda	Skorohod	Mackenzie	Venkatachari & Raj	Helle et. al. 2nd stage
$\frac{(1-\theta)^{5.26}}{b\theta^{\alpha}}$	$\frac{27(1-\theta)^{\frac{2}{m+1}}}{3\theta}$	$\frac{2(1-\theta)^3}{3\theta}$	$\frac{2}{3}\left(\frac{1-\theta^m}{m\theta^m}\right)^{\frac{2}{m+1}}$	$\frac{\ln(\theta)+0.5(1-\theta)(3-\theta)}{b(\theta-1)}$	$\frac{1-\theta}{b\sqrt{\theta}}$

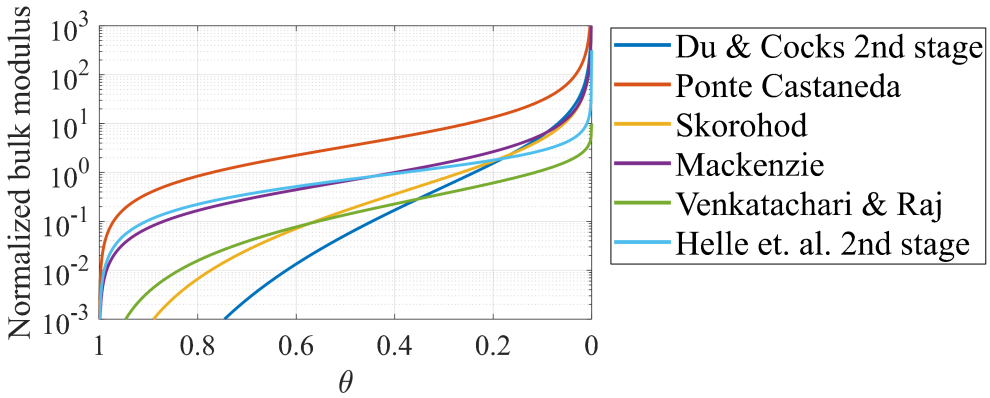

Figure 8. Expressions for the normalized bulk viscosity as function of porosity from different models (b=1 and m=1 are assumed for the calculations) [88].

Essentially, the normalized viscosities are dimensionless expressions that determine the influence of the porous structure characteristics on the effective properties of the material. Effective viscosities are obtained by combining the normalized expressions with the temperature-dependent shear viscosity of the powder material η_0.

Different expressions, including polynomial and exponential functions, have been used in the literature to represent the solid material's shear viscosity (η_0). For metallic polycrystalline materials, however, the sintering process is primarily driven by thermally activated diffusion mechanisms. This makes the Arrhenius function a natural choice for modeling the viscosity evolution, which previously has demonstrated good agreement with experimental observations [96]:

$$\eta_0 = A_0 T exp\left(\frac{Q}{RT}\right) \tag{6}$$

where T is the temperature, A_0 is the pre-exponential term and Q is activation energy.

The last term P_L represents the driving force behind sintering related to the reduction of free surface energy. This translates into a sintering stress that acts on the viscous material, pulling it together and causing densification of the continuum media without requiring external pressure. The sintering stress is expressed as a function of the porosity θ, the particle size r_0, and the surface energy of the powder material α as follows:

$$P_L = 3\alpha \frac{(1-\theta)^2}{r_0} \tag{7}$$

Initially, models estimated sintering stress based on the average particle size. However, this disregards the significant impact of grain size on densification kinetics. Grain size directly affects both the length of diffusion paths and the capillary forces driving sintering [62,97,98]. Consequently, grain growth deteriorates densification of the powder specimen, particularly at low porosities, when grain boundaries separate from the pores. To include this effect, the grain growth kinetic can be incorporated into the sintering stress as $r_0 = G/2$, where G is equivalent the grain diameter. Furthermore, the following grain growth kinetic equation [10] also accounts for the pinning influence of pores at high porosity levels:

$$\frac{dG}{dt} = \frac{k_0}{3G^2}\left(\frac{\rho_c}{2-\rho_c-\rho}\right)^{3/2} exp\left(\frac{-Q_G}{RT}\right) \tag{8}$$

where k_0 is the pre-exponential term, Q_G is the activation energy and ρ_c is a critical porosity that accounts for the transition between porosity influenced and normal grain growth.

Finally, the porosity evolution during sintering is driven by the mass conservation law, which is described as a function of the volumetric shrinkage rate as follows:

$$\frac{\dot{\theta}}{(1-\theta)} = \dot{\varepsilon}_x + \dot{\varepsilon}_y + \dot{\varepsilon}_z = \dot{e} \tag{9}$$

CHAPTER 5: MATERIALS AND METHODS

5.1 Materials and manufacturing process

The samples and components used in this study were manufactured using binder jetting (BJT). During this thesis study, two different combinations of BJT system and 316L stainless steel powders were used for the samples manufacturing. Samples A were printed using a Digital Metal® printer and DM 316L powder, while samples B were printed using a ExOne® Innovent + printer and Osprey® 316L powder (detailed in Table 2). In both cases, the standard aqueous-based organic binder provided by the BJT system manufacturer was used. After printing, the powder box was cured in an oven and the parts were extracted during the depowdering process. The details of the curing and debinding step depend on the BJT system used and are described in Table 4.

Table 2. Details of the binder jetting systems used for the printing of green parts

	DM P2500	**ExOne Innovent +**
BJT printer		
Build volume	203 x 180 x 69 [mm]	160 x 65 x 65 [mm]
Layer thickness	42 μm	50 μm
Powder material	DM 316L (D_{10} = 8 μm; D_{50} = 16 μm; D_{90} = 26 μm)	Osprey® 316L (D_{10} = 3.5 μm; D_{50} = 9.7 μm; D_{90} = 20.9 μm)

Table 3. 316L powder chemical composition (wt.%)

Powder	**Cr**	**Ni**	**Mo**	**Mn**	**Si**	**C**	**P**	**S**	**O**	**N**	**Fe**
DM 316L	17.1	11.5	2.2	1.30	0.70	0.024	-	0.006	0.049	0.090	Bal.
Osprey® 316L	16.7	10.4	2.1	0.92	0.53	0.04	0.02	0.01	0.124	0.121	Bal.

Table 4. Different curing and debinding processes applied during the experimental process

Paper	Curing process	Debinding process
I, II	12 h at 200 °C in low vacuum achieved with a membrane pump connected to the curing furnace	Debinding step combined with sintering: 460°C for 2h in reducing atmosphere (H_2)
III, IV, V, VII	3h at 200°C in an oven without protective atmosphere	Debinding at 345°C for 3h in an oven without protective atmosphere
VI		Debinding at 640°C

Computational thermodynamics calculations were used to reveal the stability of phases during the high sintering temperature range, indicating where the δ-ferrite and liquid phases may form. Figure 9 shows the results from calculations using the composition of the powder 316L alloys detailed in Table 3. The lowest temperatures at which δ-ferrite is in equilibrium of 1310 °C and 1330 °C was obtained for the DM 316L and Osprey® 316L, respectively. Also, the DM 316L composition leads to ~7 % higher maximum δ-ferrite fraction. Possibly the lower values of C, N and higher Cr (despite the higher content of Ni and Mn) leads to the higher stability of the δ-ferrite phase. The differential scanning calorimetry results for the DM 316L powder is also shown on Figure 9 (a). During the DSC measurement, powder was heated at 10 °C/min up to 1550 °C under Ar atmosphere. The heating curve reveals that 316L powder starts melting at ~1430°C, following the transformation $\gamma + \delta \rightarrow L$.

(a) DM 316L

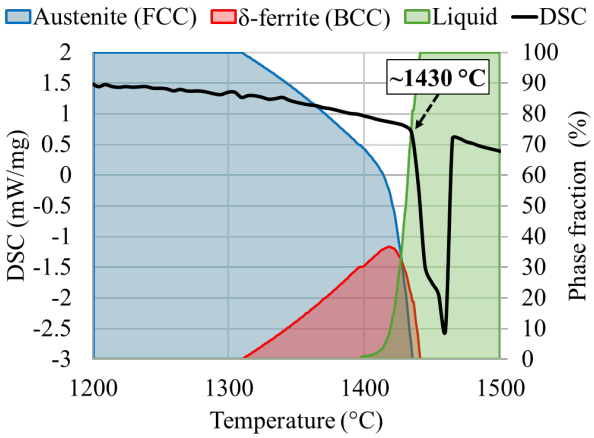

(b) Osprey® 316L

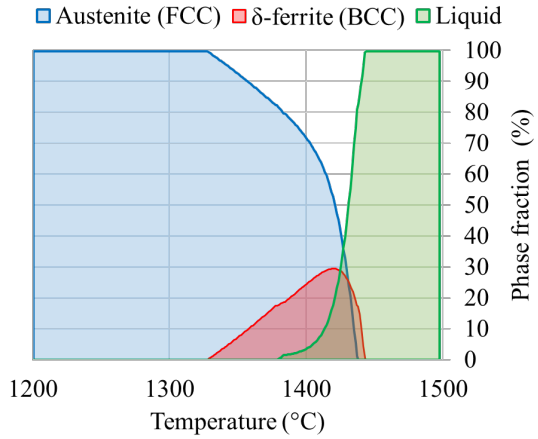

Figure 9. Calculated equilibrium phase transformations for alloys: (a) DM 316L together with DSC thermogram (black line); (b) Osprey® 316L.

5.1.1 BJT samples and components design.

Cubic samples (10x10x10 mm^3) were fabricated using both BJT systems as shown in Figure 10. Samples were oriented within the build space with their sides perpendicular to the primary printing directions: building direction (Z axis), printhead movement (X axis), and powder deposition direction (Y axis). This design permitted the measurement of distance variations between parallel planes by dilatometry, allowing for the characterization of dimensional changes related to each printing direction specified. To facilitate the cube's axis identification, each sample was marked with a numeric ID on its upper surface. Some of the as-printed cubical samples were pre-consolidated by pre-sintering in an industrial batch furnace under pure hydrogen atmosphere by heating at 5°C/min up to 900°C with a dwell time of 1 hour and final furnace cooling down to room temperature. These samples were used for the fundamental characterization of the sintering process. The use of debinded or pre-sintered samples for further dilatometry experiments will be indicated for each case. Then, the data collected were further analyzed and post-processed for the identification of model parameters.

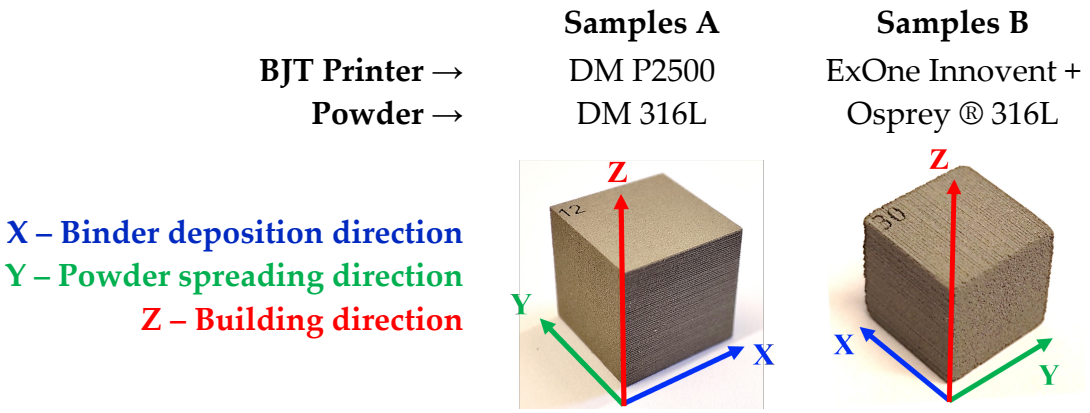

Figure 10. Cubic samples (10x10x10 mm^3) printed using each combination of BJT systems and 316L powder.

Various demonstrator components were designed to demonstrate the degree of shape deformation and densification of BJT components during the sintering process (Paper VII). Figure 11 shows the as-printed (green) demonstrator components printed with the DM P2500 BJT system. Two distinctive "tree-like" geometries were designed, each featuring three branches composed of straight overhangs. The thickness of the overhangs are 3 mm (Figure 11 (a)) and 2 mm (Figure 11 (b)) for each designed geometry, and their lengths progressively decrease from bottom to top, measuring 20 mm, 15 mm, and 10 mm. Additionally, a second set of four different geometries was designed, showcasing overhangs at varying angles and lengths. The first group exhibits overhang beams angled at 75°, 45°, and 15°, with lengths of 13 mm (Figure 11

(c)) and 10 mm (Figure 11 (d)). The second group displays overhang beams angled at 90°, 60°, and 30°, also measuring 12 mm (Figure 11 (e)) and 10 mm (Figure 11 (f)).

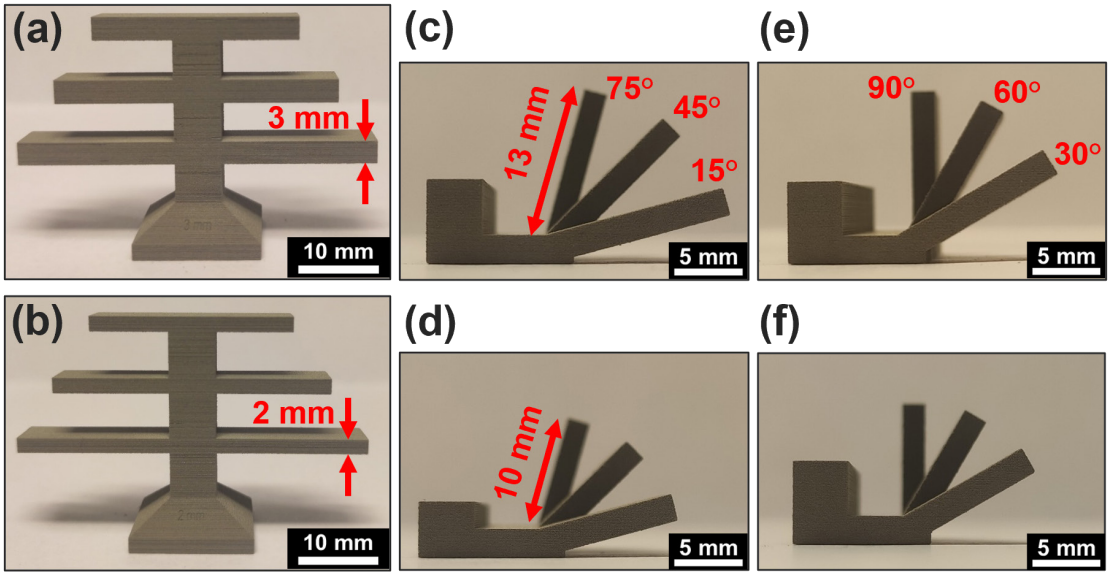

Figure 11. As-printed (green) demonstrator components.

Also, different engineering BJT components were studied in collaboration with researchers at University of Trento (Paper VI). The components consist of three different variants (G1, G2 and G3) of tee connector based on the geometry shown in Figure 12, varying the size of the horizontal and vertical connection cylinders. The X, Y, and Z axes of the geometry (see Figure 12) also correspond to the binder deposition, powder spreading and building direction, respectively. The CAD geometry of these components was scaled up to compensate for the densification shrinkages using scaling factors provided by the manufacturer.

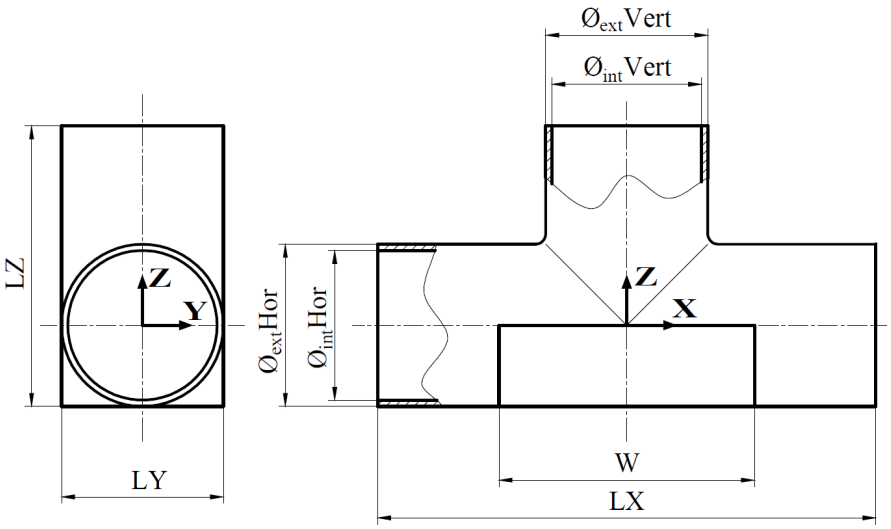

Figure 12 Designed tee connector geometry, indicating the relevant dimensions of the component.

5.2 Material Characterization

5.2.1 Dilatometry (DIL)

Dilatometry is an extremely precise technique that monitors the dimensional changes of a sample as a function of temperature and time. This valuable method is widely employed to investigate various phenomena, encompassing sintering densification shrinkages, thermal expansion and contraction behavior, and dimensional alterations induced by microstructural phase transformations.

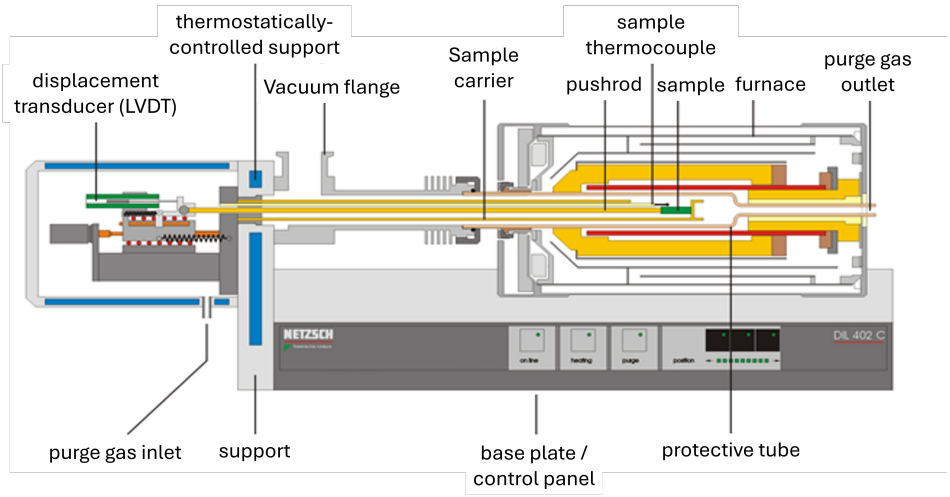

Figure 13. Illustration of the Netzsch DIL 402C dilatometer (with permission).

The instrument used for the experiments presented in this thesis study is a vacuum tight dilatometer DIL 402C from NETZSCH (NETZSCH-Gerätebau GmbH, Germany) equipped with W-Re thermocouple for inert or reducing atmosphere. It employs a displacement transducer to convert the linear movement of the sample into precise measurement signals, providing a resolution of 1.25 nanometers/digit. The dilatometer chamber, equipped with a rotary pump and a turbo pump, enables sintering in high vacuum environments, reaching pressures as low as 10^{-5} mbar. To eliminate the influence of residual air, the instrument undergoes a rigorous purging process before each measurement. The samples were placed on an alumina support and in contact with the pushrod with a force of 30 cN. Experiments were conducted under a continuous flow (100 ml/min) of high-purity hydrogen gas (>99.9999%) to maintain a suitable reducing atmosphere.

5.2.2 Metallographic preparation

The metallographic preparation of the materials was performed following different methodologies, depending on the porosity level of the sample and the geometry. The cubical samples were cut along three different cross-sections parallel to the external

planes of the cube. The corresponding cross section is typically identified with the two cube's axes that define the cutting plane: XZ, YZ or XY. After cutting, two different mounting methods were used depending on the porosity level. In general, hot mounting using Citopress-20 (Struers) and a conductive resin PolyFast (Struers) was done for samples with high density (≳ 90%). On the other hand, for samples with lower density and potentially large open porosity, cold mounting was done using a vacuum impregnation unit Citovac (Struers). EpoFix resin (Struers) was used due to its low viscosity and low shrinkage after curing. Curing was performed in the oven at 40 °C during 12 h. Finally, the mounted samples were prepared by grinding and polishing following guidelines for PM stainless steel materials. Coarse grinding was followed by mechanical polishing using 9 μm, 3 μm and 1 μm suspended diamond solutions. Then, additional preparation steps were tailored for each specific characterization requirements:

- **EBSD analysis (SEM):** final polishing step was performed using colloidal suspension of silica particles (~50 nm) on an oxide polishing cloth followed by careful cleaning of the sample surface.
- **Grain boundaries (LOM):** Electrochemical etching with 40% nitric acid (HNO_3) solution was performed. This solution was especially suitable for grain size measurements due to its ability to reveal grain boundaries while preventing the etching of twin boundaries.
- **Delta-ferrite phase:** Electrochemical etching with 40% sodium hydroxide (NaOH) solution is done to reveal this phase.

5.2.3 Light optical microscopy

Light optical microscopy (LOM) is a widely used technique utilized in the field of materials science. The resolution of LOM is limited by the wavelength of visible light, which restricts its ability to image smaller features. However, it is still sufficient for studying the features present in the microstructure of powder metallurgy components, particularly those produced using micron-sized powders, such as those used in binder jetting. It allows for the 2D characterization of porosity in cross-sectional images, which can help to identify and quantify pores and evaluate their distribution. The Zeiss Axioscope 7 Light Optical Microscope (LOM) equipped with Zeiss Axiocam 105 color camera was used to collect images of the samples studied. This optical microscope includes a powerful stitching feature that enables to combine multiple images of a specimen into a single, high-resolution image. This is particularly beneficial for imaging large or complex specimens that cannot be captured in a single field of view. Then, the FIJI ImageJ software [99] was used for performing the density measurements and porosity analysis [100].

5.2.4 Scanning electron microscopy

When higher resolution is required, scanning electron microscopy (SEM) is typically employed instead of conventional light optical microscopy (LOM). SEM operates by generating an electron beam from an electron gun (field emission or tungsten filament), which is then focused onto the sample surface using electromagnetic fields and lenses. The electrons interact with the sample, emitting various types of signals, including secondary electrons (SE), backscattered electrons (BSE), and X-rays. These signals are then collected by different sensors and used for various analytical purposes. Typically, the SEM systems can be equipped with different types of tools and detectors that allow for advanced analysis and manipulation of the samples. For instance, the Electron Backscatter Diffraction (EBSD) technique can be utilized, which enables the acquisition of information about the material's internal lattice structure. This information includes the crystalline phases present, the distribution of grain sizes, the properties of grain boundaries, crystallographic textures, and local strain variations.

The scanning electron microscopes Zeiss Leo 1550 and GeminiSEM 450 were used for microstructural characterization. The crystallographic information was gathered by the EBSD technique and data were postprocessed by using open-source MTEX module [24] and AztecCrystal (Oxford instruments) software. In general, EBSD measurements were conducted with a step size of 0.5 μm and an acceleration voltage of 20 kV. Post-acquisition, the resulting datasets were refined by using a noise reduction tool. The high angle grain boundaries (with a misorientation ≥10°) were displayed as black lines, and the twin boundaries identified with a misorientation angle of ~60° were displayed as white lines in the EBSD maps. Black regions in the maps indicate non-indexed data, typically associated with the pores in the material.

5.2.5 Density measurements and porosity analysis

To assess the porosity of the additively manufactured BJT samples [100], this study employed three different density measurement methodologies depending on the state of the sample:

- **Geometry-based density ($\boldsymbol{\rho_{Geom}}$)** was calculated for the cubical samples before and after sintering. The measured weight (w) and volume ($V = L_X + L_Y + L_Z$) from caliper measurements were used to calculate the relative density as follows: $\rho(\%) = \frac{\mathrm{w}}{\mathrm{V} \cdot \rho_{full}} \cdot 100$, where $\rho_{full} = 7.95\, g/cm^3$. For the demonstrator geometries, the CAD file volume was used for the calculation.

- **LOM-based density (ρ_{LOM})** was obtained by thresholding the grayscale image obtained by Light Optical Microscopy and calculating the area fractional density.
- **Archimedes density (ρ_{Arch})** was measured following the standard method ASTM B962−17 [101]. The Archimedes density was done using wax impregnation for the low densified samples with open porosity (typically below 90 %).

A manual caliper with a resolution of 0.01 mm and high precision balance with a resolution of 0.0001 g were used for the measurements.

5.2.6 Grain size characterization by LOM and EBSD

For the systematic grain sizes measurements, a particular methodology was implemented, based on the utilization of LOM and EBSD measurements as illustrated in Figure 14. Sample cross-sections along the three orthogonal planes (XZ, YZ, XY) were used to acquire 25 LOM images at 200x magnification, evenly distributed throughout the sample. Then, images were post-processed using Fiji software for binarization and removal of internal pores within the grains. Binary images were used to measure the line-sampled linear intercept length method implemented in MATLAB ® [102]. The linear intercept lengths are typically adjusted by a factor ~1.5 to represent the grain size [103]. However, the factor $k_G = 1.417$ used in this thesis was derived from the comparison between equivalent circle diameter from EBSD and the linear intercept length measured from the same sample [104].

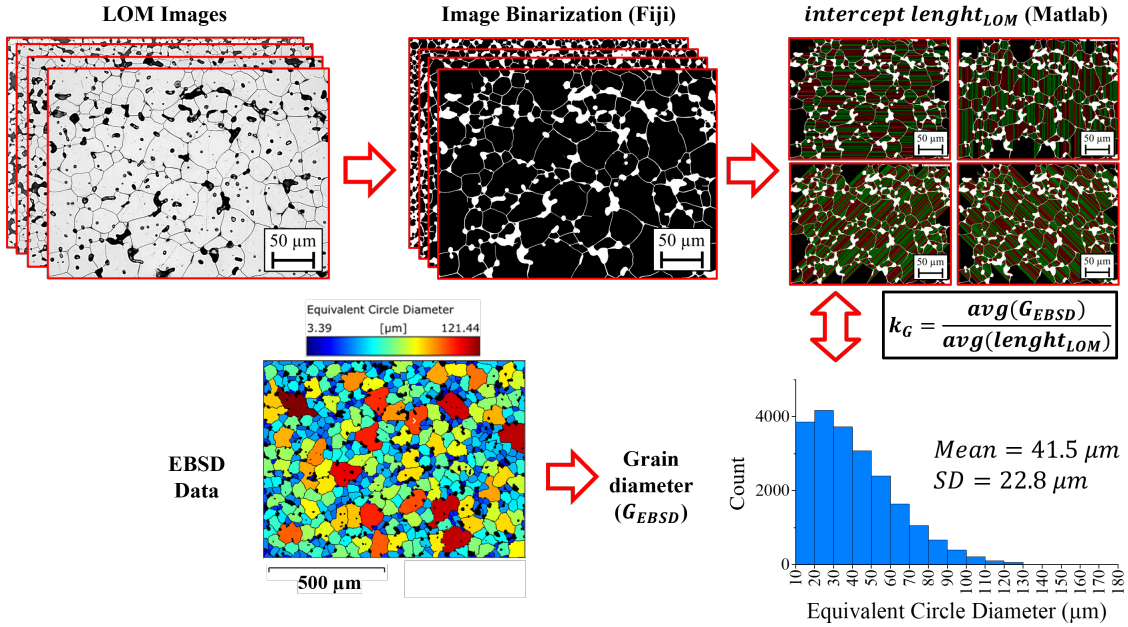

Figure 14. Schematic of the method used for the calculation of the average grain size of sintered samples by image analysis and EBSD [104].

5.2.7 Synchrotron X-Ray Computed Tomography (SXCT)

The SXCT experiments were conducted at the BAMline, BESSY II (Berlin, Germany) by the co-authors of the study. The reconstruction of 3D volumes, denoising and filtering was made by BAM in-house developed software. After acquisition, each dataset underwent post-processing, involving cropping and thresholding, to isolate the two relevant phases (solid and porous) within the 3D volume. This resulted in binary datasets with a voxel size of 0.7 μm, suitable for comprehensive microstructural analysis. The 3D renderings of the data were generated for the qualitative evaluation. For quantitative analysis, the 3D data was subjected to sequential 2D slicing as detailed in [44]:

- Slicing along the building direction (Z axis): a sequence of horizontal 2D slices perpendicular to the building direction were extracted for each sample. The area density $\rho_z = f(z)$ was measured along the vertical direction.
- Slicing along different angled directions contained within the horizontal printing plane (XY plane): series of vertical planes were extracted for each sample, defined by the building direction and a perpendicular direction defined by an angle α. For each angle and orthogonal position x_α, the 2D slice was extracted and its plane area density $\rho_\alpha = f(x_\alpha)$ was measured. Note that the specific X and Y axis cannot be identified in the 3D data due to the cylindrical symmetry of the volume scanned.

CHAPTER 6: SUMMARY OF APPENDED PAPERS

In this chapter, the research questions (RQ) previously presented in section 1.2 are addressed by summarizing and discussing the results from appended manuscripts. Some other relevant results not contained in the papers have also been included in this chapter. The first section **6.1** addresses the study of the shrinkages caused by densification during sintering of BJT 316L by dilatometry experiments (**RQ1**). Then, section **6.2** is focused on the evolution of the microstructure (e.g. pore distribution, grain size, phases, etc.) during the sintering process of BJT samples and its connection with the densification shrinkages (**RQ2**). The third section **6.3** describes the phenomenological continuum modeling of sintering, specifically discussing the main parameters studied and its identification for the stainless steel BJT components (**RQ3**). The fourth section **6.4** compiles the sintering simulation results of real engineering components and demonstrators that reveal the accuracy and applicability of the sintering model developed by its comparison with the sintered BJT components (**RQ3** and **RQ4**).

6.1 Densification shrinkages of BJT components during sintering

The impact of the binder burnout during the debinding step on the dimensional changes was investigated using green samples B (see 5.1.1), where de-binding step was included in the dilatometry experiments. Figure 15 (a) shows the dimensional evolution obtained from dilatometry experiments using green and pre-sintered samples B during the heating stage (from RT up to 1370 °C at 5 °C/min). It is evident that the green component experience minor shrinkages prior to the sintering onset temperature (~900 °C), while the pre-sintered sample mainly undergoes thermal expansion. Besides, Figure 15 (b) shows the evolution of shrinkages during debinding and heating up to 900°C of green samples sintered along the different sample's axes X, Y and Z by dilatometry. These results reveal analogous minor shrinkages (< 0.5 %) which can be related to small rearrangement of particles caused by the binder removal.

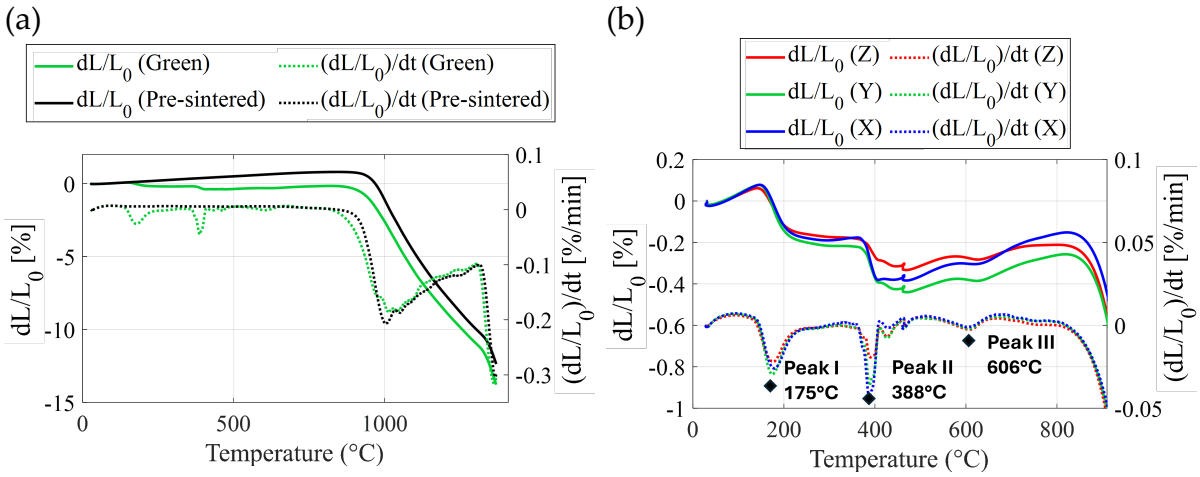

Figure 15. Dimensional evolution of samples B during debinding: (a) comparison between pre-sintered and green samples shrinkages during heating, (b) multi-axial debinding shrinkages [105].

Figure 16 shows the shrinkages from pre-sintered samples B, sintered at (a) 10 °C/min up to 1300 °C for 1 h and (b) 5 °C/min up to 1370 °C for 1 h. Both results show consistent larger shrinkages along the Z axis (building direction). After the sintering onset (~943 °C) and during the heating step, shrinkages progression is almost steady until a temperature of ~1315 °C, see Figure 16 (b). Above this temperature, the shrinkage rate increases significantly due to the boosted densification caused by microstructural changes. Specifically, the formation of δ-ferrite phase enhances the sintering diffusion mechanisms, boosting the densification and the related shrinkage behavior [45,64,66,105–107]. The stability of this phase above the observed temperature was also revealed by the phase diagrams in Figure 9. This phenomenon will be discussed in detail during the next section 6.2.

Anisotropy factors calculated from the ratio between the shrinkages reveal increases up to a final value of ~1.15 for the sintering cycles studied [105]. Similar behavior has been frequently observed in different studies [108–111], with anisotropy factors ranging between 1.13 to 1.3. However, to uncover the correlation of anisotropy with densification, the difference between Z-Y and Z-X axis shrinkages in Figure 16 was plotted against the porosity calculated following the mass conservation equation (9). This data reveals a linear relationship between the densification and the evolution of shrinkages anisotropy, starting from the onset of sintering. In these samples, the boosted densification above ~1315 °C does not notably impact the evolution of the anisotropy. Additionally, these samples experience a substantial density increase (~25 %) already below this temperature.

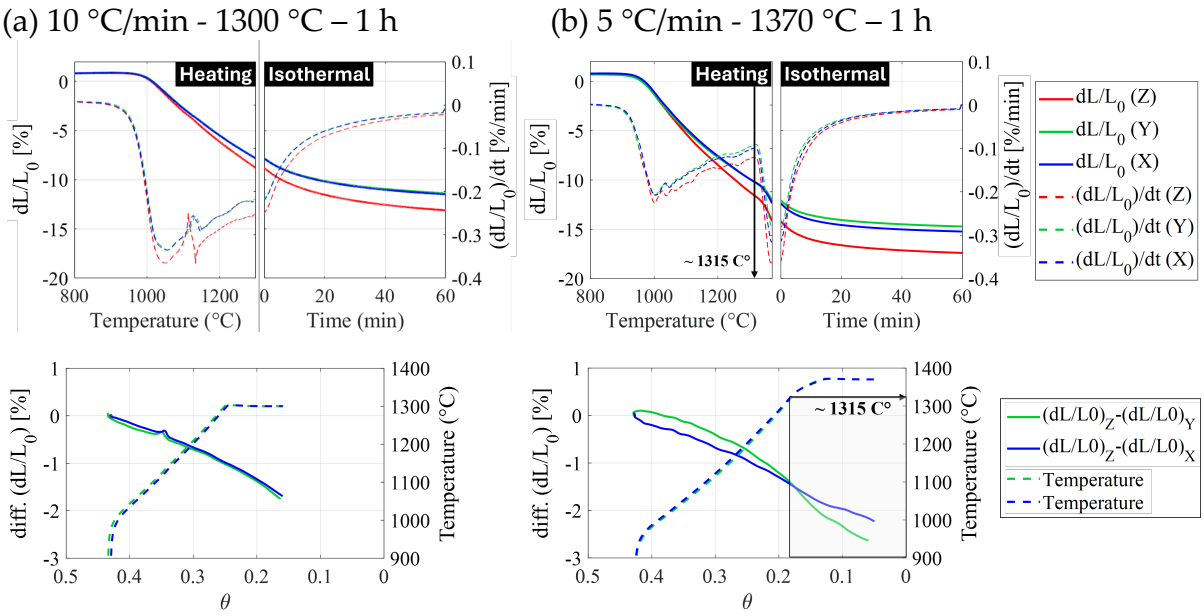

Figure 16. Multi-axial sintering shrinkages from dilatometry experiments of samples B aligned along Z axis, Y axis and X axis (top) and shrinkage differences as function of densification (bottom): (a) 5 °C/min heating up to 1370 °C, and (b) 5 °C/min heating up to 1370 °C [105].

Pre-sintered samples A (see 5.1.1) were also subjected to multi-axial sintering studies. Figure 17 (b) reveals the results from samples sintered at (a) 10 °C/min up to 1300 °C for 1 h, and (b) 5 °C/min up to 1370 °C for 1 h. These samples also exhibit larger shrinkages along the Z axis (building direction) when subjected to sintering at the highest temperature of 1370 °C for 1 h. However, Figure 17 (a) reveals practically isotropic shrinkage behavior and significantly lower shrinkages when sintering was done at lower temperature (1300 °C for 1 h). The shrinkages anisotropy during heating is minimal, and mostly increases during the isothermal step at 1370 °C. In general, a maximum final shrinkage anisotropy factor of ~1.07 was observed for samples A. Then, a steady shrinkages progression can be observed until a temperature ~1310 °C, followed by a strong shrinkage rate increase until the end of the heating step. The Z-Y and Z-X shrinkages difference from samples A were plotted against the porosity in the bottom graphs of Figure 17. The anisotropy development here is delayed until a higher temperature, analogous to the temperature of the increase on shrinkage rate observed previously. Moreover, a large extent of the densification (~27 %) occurs above this temperature.

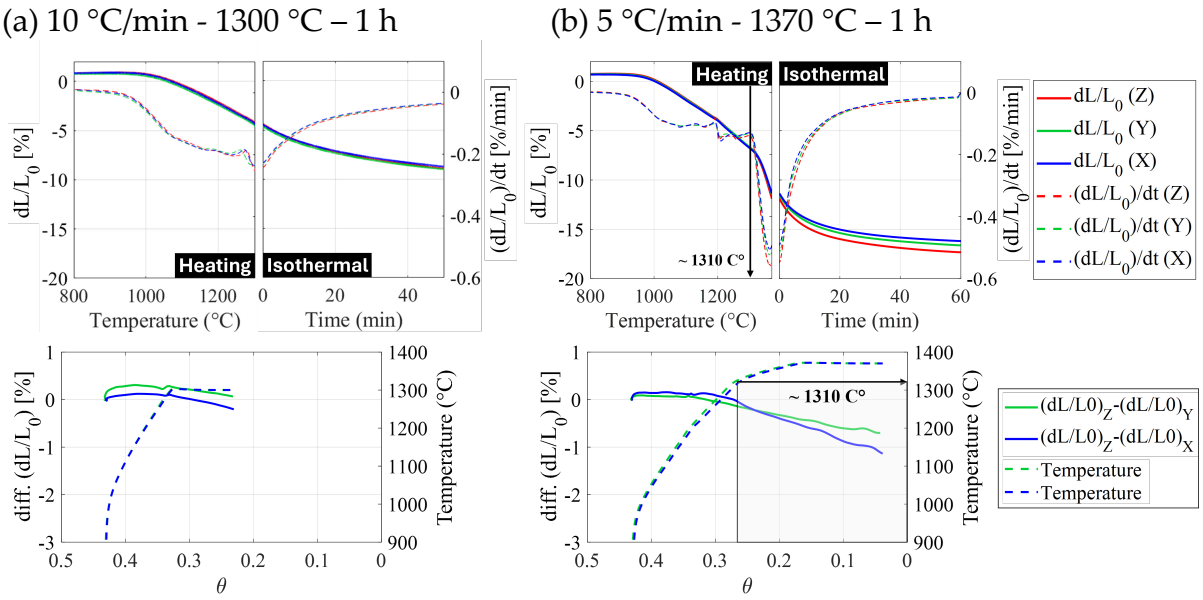

Figure 17. Multi-axial sintering shrinkages from dilatometry experiments of samples A aligned along Z axis, Y axis and X axis(top) and shrinkage differences as function of densification (bottom): (a) 5 °C/min heating up to 1370 °C, and (b) 5 °C/min heating up to 1370 °C [105].

The increased shrinkage rate above ~1310 °C was clearly observed in Figure 17, but seems to be limited by the end of the heating step. Therefore, interrupted dilatometry sintering experiments results at several temperatures between 1300 °C and 1420 °C are shown in Figure 18, revealing more details of the boosted densification behavior. The shrinkage rate peak was found at ~1366 °C, revealing that beyond this temperature the increase on densification rate fades. Therefore, 1370 °C is a suitable temperature for the sintering process of this material.

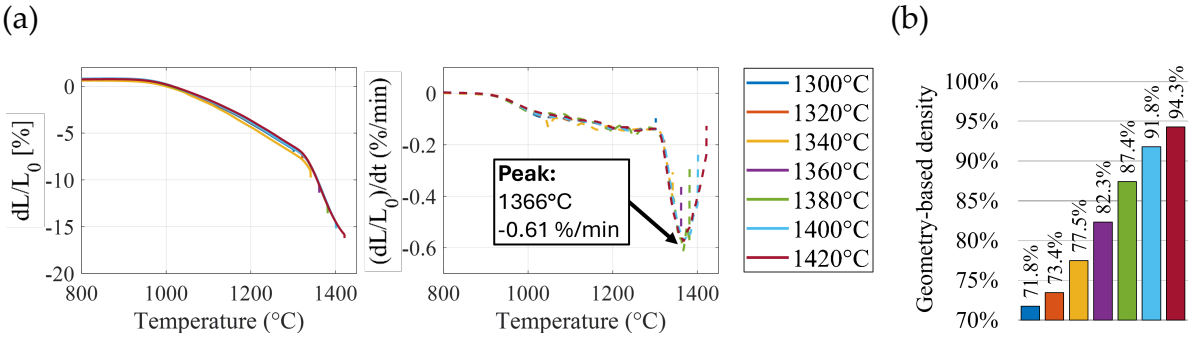

Figure 18. (a) sintering shrinkage and shrinkage rate from interrupted dilatometry sintering experiments at several dwell temperatures (1300 °C to 1420 °C) using samples A. (b) measured geometry-based sintered density.

The results presented in this section disclose the connection between the shrinkages along different printing directions and the densification process. A consistent tendency of larger shrinkages along the building direction (Z axis) was observed in both sample sets analyzed, which agrees with previous studies ([2,7,21,59,108–112]). Furthermore, this dependency seems to be potentially connected to the powder and

BJT printing process characteristics. Consequently, related to the relative density distribution and powder particle's arrangement within the green components. However, the shrinkages along the binder spreading (X) and powder deposition (Y) directions do not reveal a consistent tendency [105], and further research is required to thoroughly investigate its behavior.

6.2 Microstructural evolution during sintering

In this section, the details of the microstructure evolution during sintering of the BJT samples will be revealed and discussed by employing different characterization techniques. Figure 19 shows the XZ and XY cross-sections LOM images of the sintered samples B from the dilatometry experiments discussed in section 6.1. These images reveal the progress of pore evolution from the green interconnected porosity to small isolated quasi-spherical pores at the end of sintering. Qualitatively, the evolution of a "layered" porosity structure can be evidenced from two observations: the alignment of pores along the X direction in the XZ cross-section, and the bimodal pore distribution on the XY cross-section. This last observation is a side-effect of sample preparation, where a perfect parallel cross-section to the cube's plane is practically impossible. Nevertheless, at the end of the sintering process, the porosity distribution homogenizes and high densification of ~96 % (Geometry-based density) is reached when sintering at 1370 °C for 1 h.

Figure 19 also displays the EBSD phase maps of sintered samples B. The presence of BCC (δ-ferrite) phase was observed on the sample sintered at 1370 °C, indicating a connection between this phase formation and the increase on shrinkage rate observed in Figure 16. However, only a residual amount of the δ-ferrite existing at 1370 °C could be retained at RT due to the relatively slow cooling (30 °C/min) of the samples in dilatometer. Besides, the sample sintered at 1300 °C shows austenitic grain structure with smaller grain sizes and larger porosity.

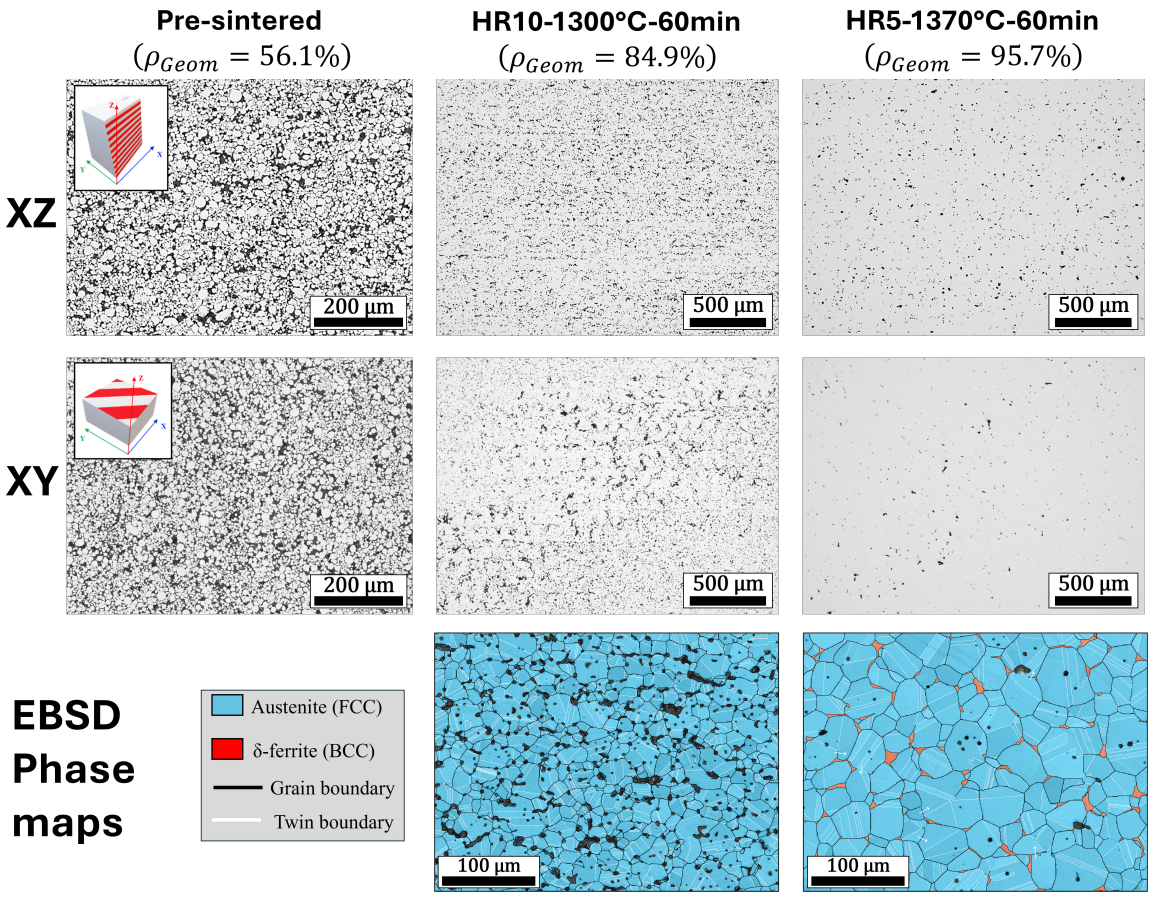

Figure 19. XY and XZ cross-sections optical micrographs of the sintered cubical BJT samples B; and EBSD phase maps where Austenite (FCC), δ-ferrite (BCC) phases and non-indexed (porosity) are shown in blue, red and black, respectively. [106].

The formation of δ-ferrite was correlated with the increase in shrinkage rates and densification. However, this transformation is highly sensitive to the alloy composition as detailed in chapter 3. Figure 20 shows the phase equilibrium calculated using the C, N and O measured in BJT samples at different stages of the process. This reveals the potential influence of these elements from the binder on the δ-ferrite and liquid phase transformation temperatures. Previous studies have shown similar effects on steel alloys [45,66]. Although the potential localization of elements caused by binder concentrated on the powder surface could theoretically affect local phase equilibrium and transformation kinetics, substantial reduction of C, N and O was observed after sintering. This suggests that the phase equilibrium likely lies between the calculated from compositions of pre-sintered and sintered samples (P-1370C) in Figure 20. Nevertheless, the powder composition may serve as a starting point for predicting the phase evolution of BJT components during sintering.

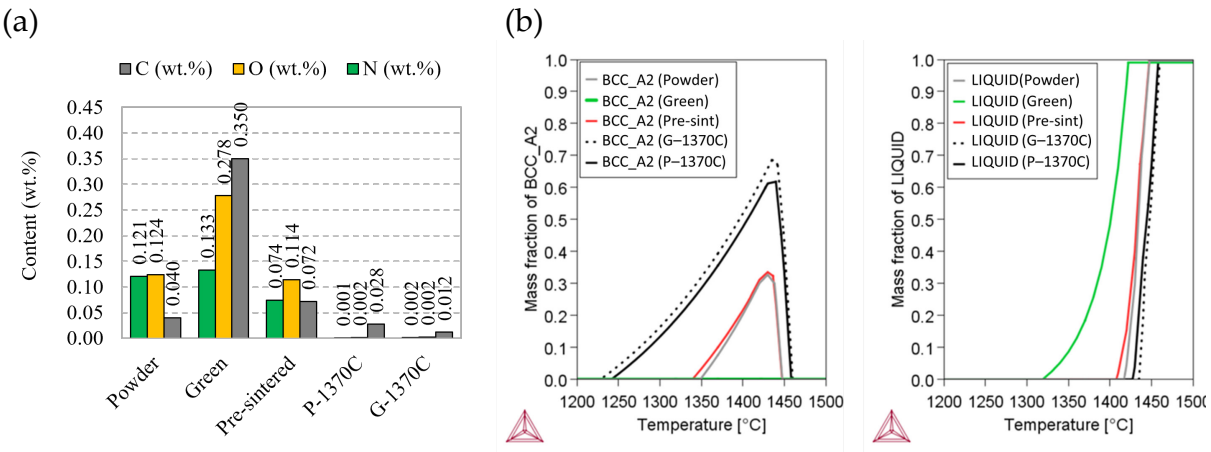

Figure 20. (a) Bulk content of C, O and N for 316L powder, BJT green sample, pre-sintered and sintered samples. (b) δ-ferrite and liquid phase equilibrium fractions as function of temperature [106].

The cubical samples A studied by dilatometry (see Figure 17) were also characterized by optical microscopy. Figure 21 shows the LOM XZ and XY cross-sections images of pre-sintered and sintered samples. Qualitatively, the particle size distribution in the pre-sintered samples appears to be relatively narrower than the previous samples. Also, signs of the layered porous structure emerge, with pores aligned along the X-axis in the XZ cross-section and regions of larger pores in the XY cross-section. Figure 21 shows the EBSD phase maps of sintered samples, again revealing the presence of BCC (δ-ferrite) phase in the sample sintered at 1370 °C.

The results from traditional microstructural characterization presented above are limited to the 2D analysis of the microstructural characteristics (i.e. particle and pore distribution). Thus, to unveil the details of the BJT 3D complex microstructure, ex-situ characterization of the sintering process was done by Synchrotron X-Ray Computed Tomography (SXCT). The 700 µm diameter cylindrical samples used were printed using the BJT printer and powder of samples set A. Then, SXCT data was analyzed following the method detailed in section 5.2.7. Figure 22 (a) shows the relative density increase of these samples from 57 ± 1.6% (green) up to 99 ± 0.3% after sintering at 5 °C/min until 1370 °C for 1 h. Figure 22 (b) reveals a periodic pattern of density fluctuations along the build direction, related to the BJT printing layer thickness of 42 µm, which decreased to approximately 33 µm at the end of sintering. While the porosity fluctuation amplitude did not drop significantly until 1370 °C, densification increased rapidly above 1300 °C, evident in the density increase from 73.6% to 92.7% despite a small temperature increase of 70 °C. This correlation between the amplitude drop and anisotropic shrinkage observed in Figure 17 hints at a possible connection between porous structure evolution and shrinkage anisotropy. However, further research is needed to confirm this connection and determine the underlying mechanisms.

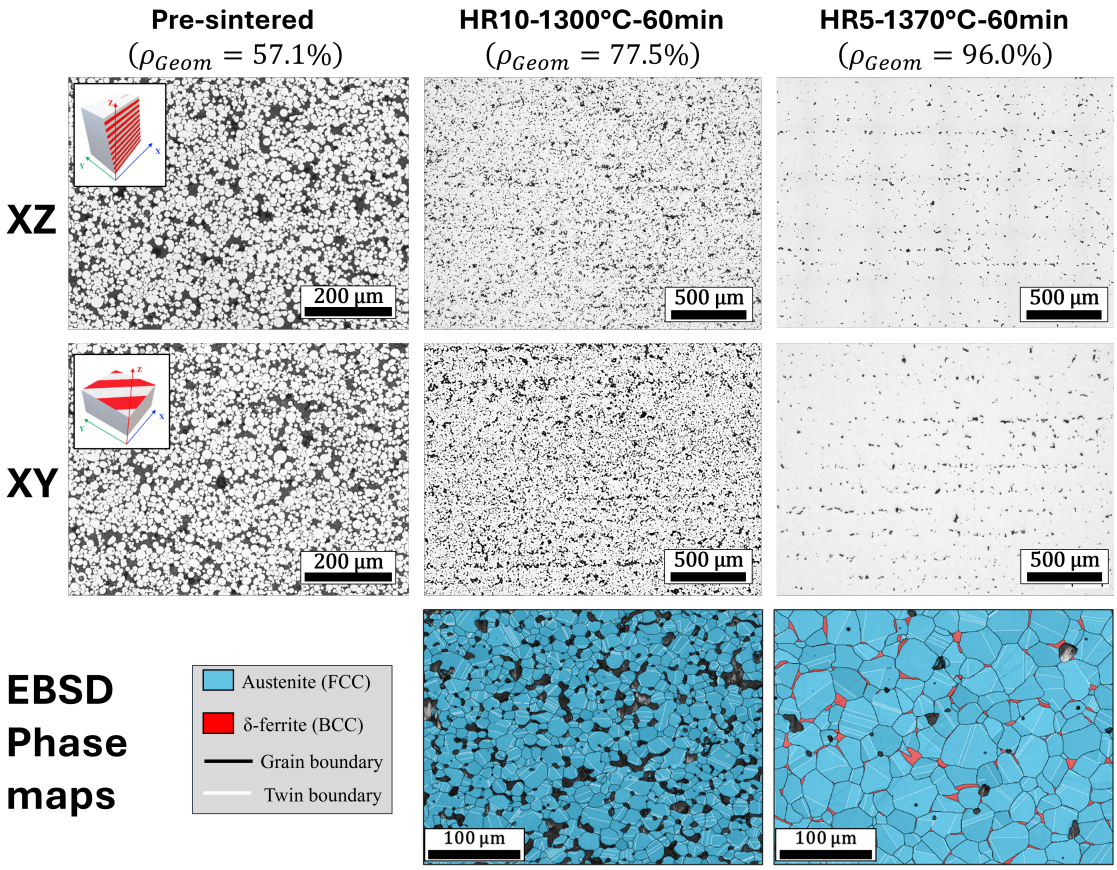

Figure 21. XY and XZ cross-sections optical micrographs of the sintered cubical BJT samples A; and EBSD phase maps where Austenite (FCC), δ-ferrite (BCC) phases and non-indexed (porosity) are shown in blue, red and black, respectively.

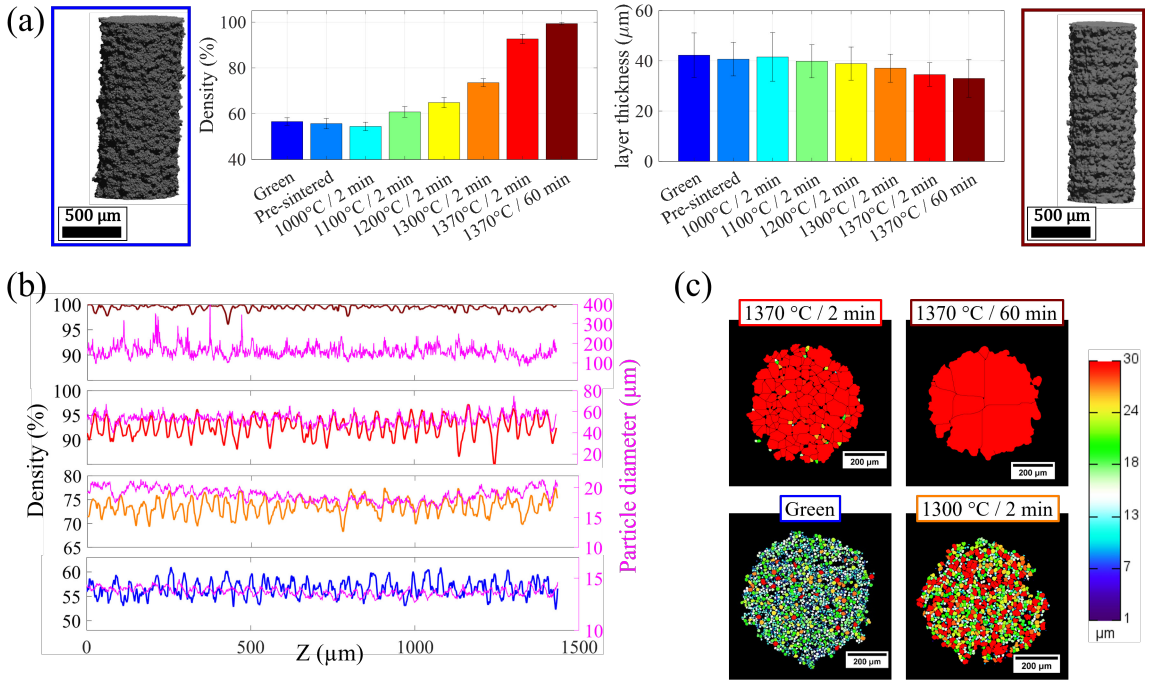

Figure 22. SXCT characterization of the BJT pin samples: (a) density and density pattern periodicity, (b) density fluctuation and segmented particle's diameter along the building direction (Z axis) and (c) XY slices extracted from the 3D SXCT datasets segmented and colored by the particle diameter [44].

To uncover the influence of the BJT printing process, the sintering behavior of the DM 316L powder was studied. Powder samples were fabricated by filling an alumina crucible (5 mm diameter and 10 mm length) with powder, followed by pre-sintering at 900 °C during 1h for pre-consolidation. Two different samples were created, one by just pouring the powder (non-tapped) and other followed by manually tapping the powder (tapped) before pre-sintering. Figure 23 shows LOM images of the pre-consolidated porous samples, revealing a difference of ~ 10% density between the fabricated tapped and non-tapped powder samples. This suggests that BJT manufactured samples (~57.1 % density) fall in between these powder arrangements configurations. In general, the sintering behavior is analogous between the BJT and powder samples as revealed by the dilatometry results in Figure 23 (sintering at 5 °C/min up to 1370 °C for 1 h). The sintered density of the powder samples is slightly higher than BJT samples. This may be related to the smaller size of the fabricated samples and differences in microstructural evolution. Moreover, the shrinkage rate increase caused by the δ-ferrite formation is shifted down ~20 °C in the powder samples and larger δ-ferrite fraction is present on the sintered microstructure (see Figure 23), which might be related to the absence of binder. Nevertheless, this comparison highlights the modest influence of the binder on the phase transformations (i.e. δ-ferrite and/or liquid) during sintering of the 316L BJT samples studied.

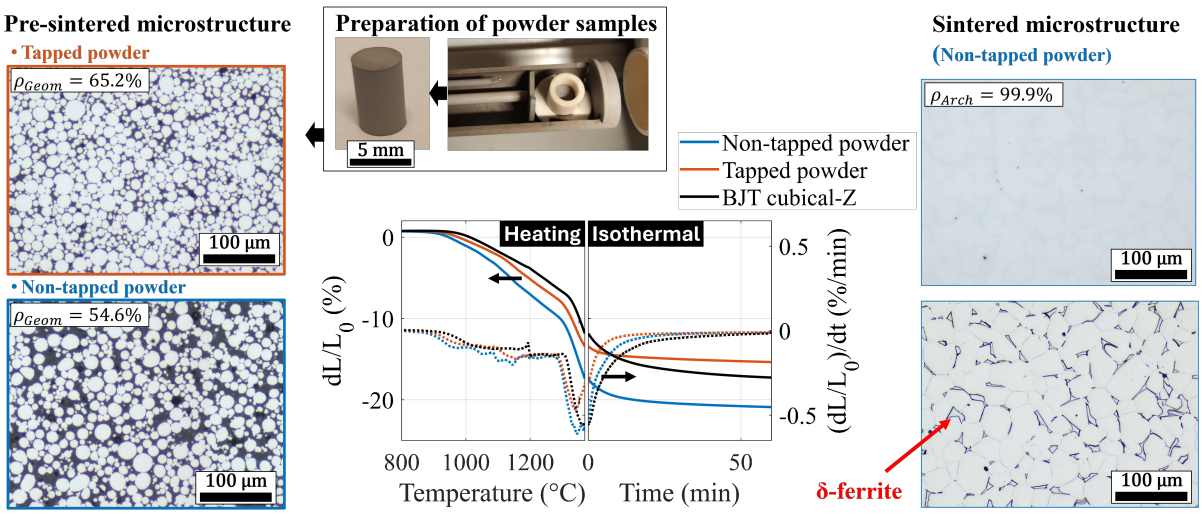

Figure 23. Sintering characterization (LOM images and dilatometry shrinkages) of samples produced by pre-sintering of tapped and non-tapped DM 316L powder.

A comprehensive study of grain growth during sintering of cubical samples A was conducted. An experimental matrix was established by sintering samples at a heating rate of 5 °C/min to temperatures of 1000, 1100, 1200, and 1300 °C and holding for durations of 2, 60, 150, and 600 minutes. The optical microscopy characterization of the samples, etched with HNO_3, is illustrated in Figure 24, together with the calculated

$(\frac{d\theta}{dt}, \theta, G)$ from mass conservation (assuming isotropy) and grain growth kinetic from equation (8). The grain sizes were calculated following the method detailed in section 5.2.6. The grain growth constants were calculated by fitting the measured grain sizes to the kinetic equation using a fitting algorithm implemented in MATLAB ® [26]. Typically, grain growth during sintering is disregarded until the final stage of sintering is reached. This is justified as the pores have a substantial influence by pinning the grain boundaries. However, significant grain growth (grain size up to ~40 µm) was observed for the sintering at higher temperatures (1300 ◦C) and longer times (600 min), despite the relatively high porosity (~10%).

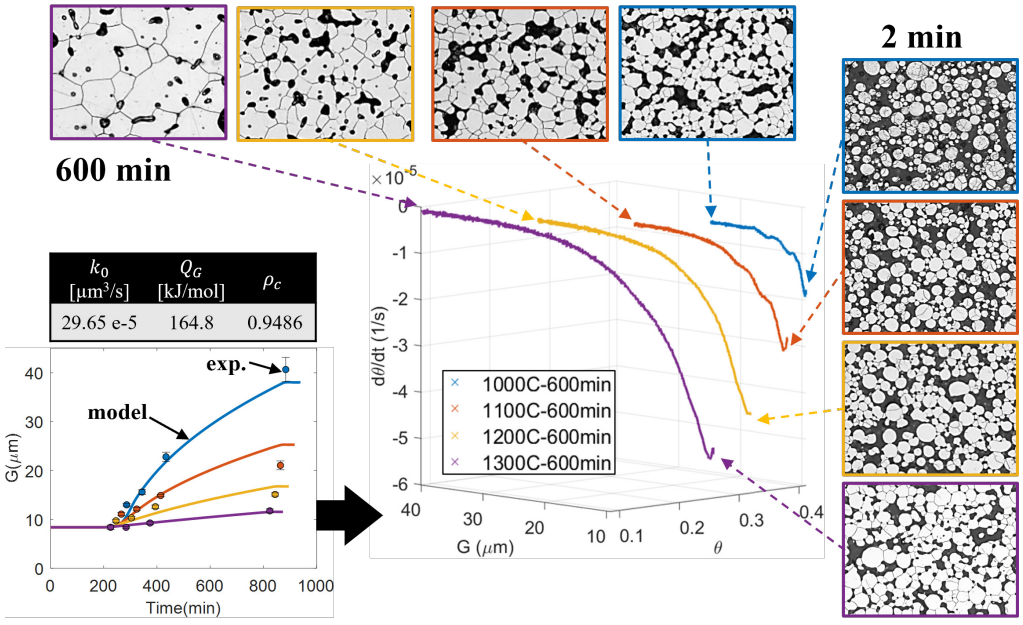

Figure 24. Sintering data $(d\theta/dt, \theta, G)$ derived from dilatometry experiments (dwell step of 600 min at 1000, 1100, 1200 and 1300°C). Also, grain growth kinetics equation fitted constants and results are shown [104].

In conclusion, the detailed microstructure characterization presented in this chapter reveals its potential correlation with the shrinkage's behavior discussed in section 6.1 and the densification during the sintering process. The layered nature of the BJT porosity distribution and its evolution during sintering was revealed. The observed progression of shrinkage anisotropy seems to be connected to the annihilation of the porous heterogeneities induced by the layer-by-layer BJT printing process. However, this complex relationship requires further in-depth investigation. Also, the δ-ferrite formation was observed on samples sintered at the highest temperature of 1370 °C for both BJT sample sets and related to a significantly increased shrinkage rate. Additionally, the grain growth behavior of the sample's set A was thoroughly characterized and modeled. The substantial amount of data collected will be used for the determination of the sintering model parameters discussed in the following sections.

6.3 Material parameters identification of the sintering model

The phenomenological model of sintering relies on the determination of the required material parameters from experimental data. These parameters are related to the sintering stress that pulls the particles together and the viscous behavior of the continuum material determined by the material, porosity, grain size and temperature [90]. The use of free-sintering processes (i.e. without applied external pressure) on the BJT manufacturing justifies the assumption of negligible external stresses. Additionally, the model assumed isotropic densification shrinkage, which could introduce significant errors for materials exhibiting strong anisotropy. Therefore, the data from samples with minimal anisotropy (samples A, section 6.1) was used for the simulation work. Following these assumptions, the constitutive equation can be simplified as follows:

$$0 = 2\eta_0 \left[\varphi \dot{\varepsilon}_z + \left(\psi - \frac{1}{3}\varphi\right) 3\dot{\varepsilon}_z\right] + P_L \tag{10}$$

Then, introducing the mas conservation law in equation (10), the following analytical expression was derived:

$$\frac{d\theta}{dt} = -\frac{(1-\theta)P_L}{2\eta_0\psi} \tag{11}$$

This last equation describes the rate of porosity change during sintering, as a function of the different model parameters. These model parameters are the normalized bulk viscosity ψ, the shear viscosity of the solid powder material η_0, and the effective sintering stress P_L. Subsequent sections will explore the characterization of model parameters for Binder Jetting (BJT) components, detailing the methodology employed for their identification.

6.3.1 Normalized bulk modulus

According to the description of the normalized bulk modulus (ψ), it should account for the particularities of the porous structure produced during the BJT printing process. For instance, the low inherent green density and the probable presence of large pores due to the printing process. Inspired on previous models of sintering, two expressions were studied, and their prediction ability was tested:

$$\psi_1(A, B, \theta) = \frac{2}{3}\frac{(1-\theta)^A}{\theta^B} \tag{12}$$

$$\psi_2(\theta_c, \theta) = \frac{2}{3}\frac{(\theta_c - \theta)^3}{\theta} \tag{13}$$

where θ is the relative porosity and A, B, θ_c are material constants related to the characteristics of the porous structure.

Apart from ψ, the parameters P_L and η_0 are required to complete the model. Therefore, incorporating the sintering stress and shear viscosity from equation (5) and (6) into equation (11) gives:

$$\frac{d\theta}{dt}G = -\frac{3}{\frac{A_0}{\alpha}Texp\left(\frac{Q}{RT}\right)} \cdot \frac{(1-\theta)^3}{\psi} = f(T,\theta) \tag{14}$$

The material constants to be identified in equation (14) are related to the material shear viscosity (A_0/α, Q) and the normalized bulk viscosity (A, B or θ_c). Then, careful evaluation and selection of the experimental data required, followed by rigorous data post-processing, are crucial for identifying these material constants.

First, the analysis of the fitting methodology was done to evaluate the relevance of gathering adequate experimental data. The results in Figure 25 (a) show that using only one experimental dataset leads to inaccurate results, as the fitting solution and model parameters are not unique and multiple surfaces can be a solution depending on the initial values of the parameters employed in the fitting process. Consequently, the outcome would fail to predict the sintering behavior under other conditions outside of the sintering treatment data (1300 °C – 600 min) used for the fitting process.

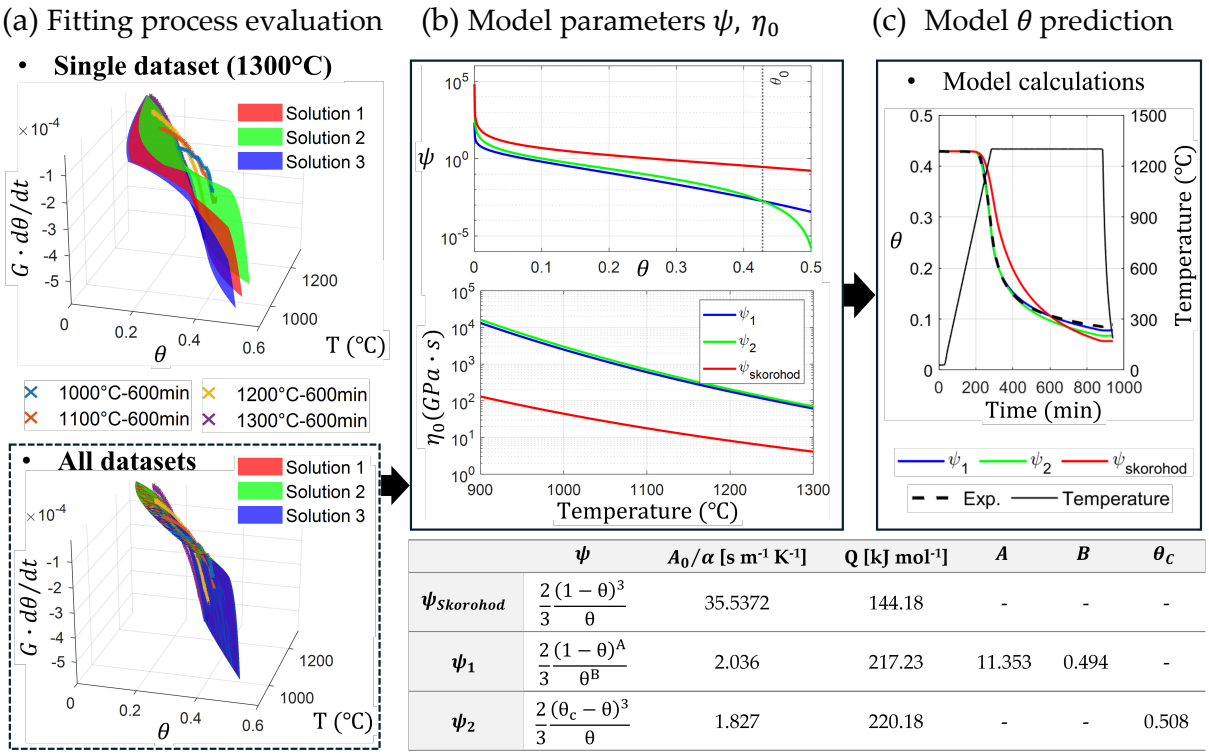

	ψ	A_0/α [s m^{-1} K^{-1}]	Q [kJ mol^{-1}]	A	B	θ_C
$\psi_{Skorohod}$	$\frac{2}{3}\frac{(1-\theta)^3}{\theta}$	35.5372	144.18	-	-	-
ψ_1	$\frac{2}{3}\frac{(1-\theta)^A}{\theta^B}$	2.036	217.23	11.353	0.494	-
ψ_2	$\frac{2}{3}\frac{(\theta_c-\theta)^3}{\theta}$	1.827	220.18	-	-	0.508

Figure 25. Process for the model parameters calculation: (a) Solutions of the non-linear least squared problems; (b) Model parameters fitted to the experimental data for each model; (c) Calculated porosity evolution from the sintering models compared with the results from dilatometry experiment [104].

Figure 25 (c) shows that the expressions ψ_1 and ψ_2 have a higher accuracy due to the use of fitting parameters that can be adjusted to the experimental data. Moreover, the

viscosity constants obtained are similar, leading to analogous evolution of the model parameters with the porosity and temperature as shown in Figure 25 (b). However, the expression ψ_1 will be further implemented in the subsequent modelling not only due to its better accuracy. Additionally, this expression allows for fine-tuning the normalized bulk viscosity at low and high densities independently. This means adjusting A primarily affects ψ_1 at higher porosities, while B does it at lower porosities. In conclusion, this phenomenological approach may have great potential for the BJT technology where the green part's porous structure and its evolution may vary substantially with the printing process used (printer system and printing parameters) and powder characteristics (powder morphology, size distribution, etc.). The following section describes the determination of the material shear viscosity accounting for the transformation of δ-ferrite phase.

6.3.2 Powder material shear viscosity: the transition from single to a dual phase microstructure.

The phenomenological model of sintering defines the material shear viscosity (η_0) as the temperature-dependent material viscosity, which is related to the combination of diffusional mechanisms occurring during the sintering process. So, it is reasonable to argue that phase transformation's influence should be comprised in this expression. Then, to find a suitable mathematical description of η_0 from the experimental data, equation (14) was rearranged as follows:

$$\eta_0 = -\frac{3\alpha(1-\theta)^3}{\psi\dot{\theta}G} \tag{15}$$

where, the densification data derived from dilatometry and calculated grain size $(\dot{\theta}, \theta, G)$, and ψ expression from section 6.3.1 are the necessary input data. Also, a surface energy of $\alpha = 1.2\ \mathrm{J}/m^2$ was assumed for the stainless steel powder [113]. Dilatometry experiments at different heating rates (2, 5 and 15 °C/min) up to 1370°C were used for the material constants identification. This first approach proposed was based on the implementation of a piece-wise function to reproduce the experimentally derived viscosity evolution with temperature, as observed in Figure 26 (a). The material viscosity function now has four material constants to be identified (A_1, Q_1, A_2, Q_2):

$$\eta_0 = A_i T\, exp\left(\frac{Q_i}{RT}\right) \begin{cases} i = 1 \rightarrow A_1\ Q_1, & if\ T < T_T \\ i = 2 \rightarrow A_2\ Q_2, & if\ T \geq T_T \end{cases}$$
$$where: T_T = \frac{Q_2 - Q_1}{R\ ln\left(\frac{A_1}{A_2}\right)} \tag{16}$$

(a) Material shear viscosity η_0 (b) Model results

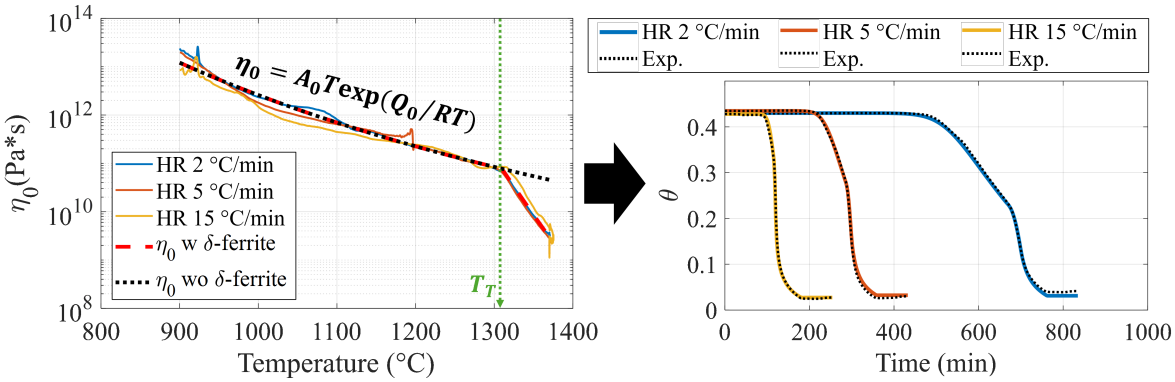

Figure 26. (a) Fitting of the material viscosity piecewise function to the experimental data. (b) Modelling results of porosity evolution during sintering and comparison with experimental data [114]. *Sintering experiments done at different heating rates (HR) up to 1370 °C and 1 h dwell time.*

Table 5. Material constants calculated by the fitting shown in Figure 26.

A_1/α $[Pa \cdot s/K]$	A_2/α $[Pa \cdot s/K]$	Q_1 $[kJ/mol]$	Q_2 $[kJ/mol]$	A	B
8.993	5.335E-32	201.7	1178.7	11.35	0.49

The prediction ability of this equation is remarkable as shown in Figure 26 (b), but the evolution of the phase fractions is not explicitly included in the model. Consequently, the material constants must be recalculated if the phase transformation is altered by changes on the alloy composition. Therefore, a new expression for the material shear viscosity was proposed, based on the concept of "rule of mixtures" and the Reuss model [115–117]. In this approach, the global strain rates are assumed to be related to the to the individual properties of the γ phase (FCC) and the δ phase (BCC) and the amount of each phase present in the microstructure, while stresses can be regarded as homogeneously distributed within the two phases. Therefore, the new expression is dependent on the individual shear viscosities ($\eta_{\gamma,\delta}$) and phase fractions (f_γ, f_δ) as follows:

$$\eta_0 = \frac{1}{\frac{f_\gamma}{\eta_\gamma} + \frac{f_\delta}{\eta_\delta}} = \frac{1}{f_\gamma / A_\gamma T \exp\left(\frac{Q_\gamma}{RT}\right) + f_\delta / A_\delta T \exp\left(\frac{Q_\delta}{RT}\right)} \quad (17)$$

For this expression, the complete fitting process was repeated for all the material constants in the model, including the normalized bulk viscosity. Then, equation (17) is fitted to the experimental data calculated by equation (15). However, the phase fraction evolution with the temperature is required to fit this expression. As initial approach, the phase fractions f_γ, f_δ obtained from thermodynamic equilibrium

calculations (JMatPro v12.4) were implemented as shown in Figure 27. This approach is justified because the phase transformation kinetics showed minimal impact on the temperature dependence of shear viscosity at the employed heating rates (2 to 15 °C). The material constants obtained are detailed in Table 6, which were implemented on (11) and used to calculated the porosity evolutions. Figure 27 (c) shows the comparison between the model predictions and the density derived from dilatometry experiments. The proposed shear viscosity expression accurately predicts the enhanced densification related to the δ-ferrite phase transformation. Furthermore, the explicit implementation of the phase fractions opens the possibility to account for alloy composition variation through the connection with thermodynamic calculations.

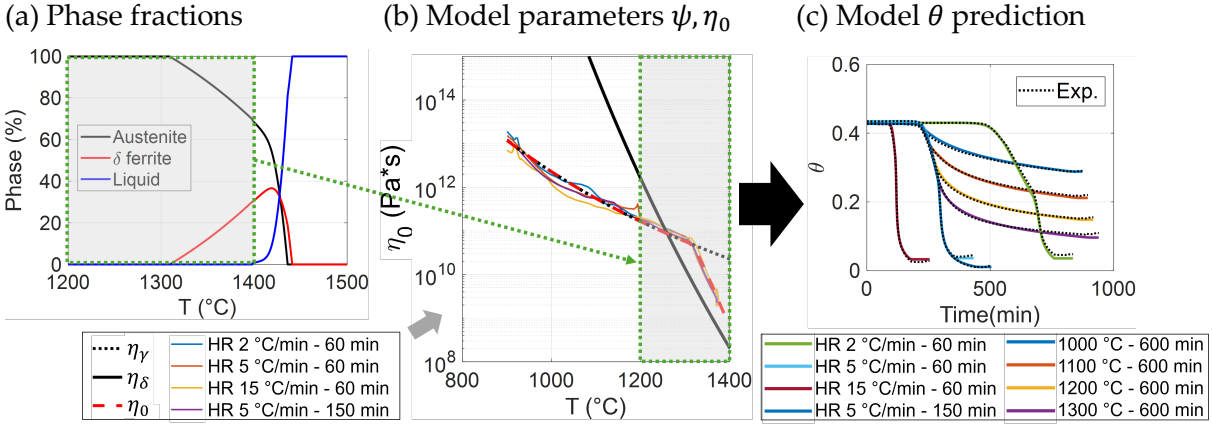

Figure 27. Fitting of the material viscosity function based on the "rule of mixtures" to the experimental data. (b) Porosity evolution calculations and comparison with experimental data. When HR (heating rate) is indicated, experiments were done up to 1370 °C. When HR is not indicated, heating was done at 5 °C/min up to the indicated dwell temperature.

Table 6. Material constants calculated by the fitting shown in Figure 27.

A_γ $[Pa \cdot s/K]$	A_δ $[Pa \cdot s/K]$	Q_γ $[kJ/mol]$	Q_δ $[kJ/mol]$	A	B
2.509	1.201E-18	215.7	738.4	11.160	0.693

6.3.3 Sintering stress

Sintering stress arises from local capillary forces at the microscopic level, driven by the surface tension of the material and the curvature of the pore surfaces. Then, individual pores experience different forces depending on their size, shape, and surrounding geometry. It is very difficult and inefficient to measure and analyze the sintering stress at the microscopic level. Instead, an effective sintering stress expression is derived, which represents the average impact of all these local forces across the entire material volume. One of the most used expressions for the sintering stress was derived based on the stochastic approach developed by Skorohod [88,95].

This expression was adapted to include the influence of grain growth into the sintering stress by replacing the $r_0 = G/2$:

$$P_L = 3\alpha \frac{(1-\theta)^2}{G/2} \tag{18}$$

The combination of porosity and grain growth calculations during sintering simulations leads to the near quadratic sintering stress evolution shown in Figure 28 (a). Sintering stress increases during early stages driven by porosity term $(1-\theta)^2$, then at some point the sintering stress starts to decrease driven by the enhanced grain growth caused by the transition to small, isolated porosity. Similar behavior was derived from the characterization of pore surface and volume by Synchrotron X-Ray Computed Tomography (SXCT) on ex-situ interrupted sintering experiments as shown in Figure 28 (b). The equation used for that purpose was derived from the definition of sintering stress as the derivative of the free energy per unit mass with respect to the volumetric mass of the porous material [88]. The sintering stress derived from the high- and low-density regions of the "layered" porosity are slightly different. Experimentally, this is probably due to differences in the pore morphology. However, in the model the difference comes from a larger θ value in the lower porosity regions, resulting in a lower sintering stress. Further analysis should be done to address the differences between these regions. However, for the purposes of larger-scale modeling, these differences appear to be negligible in this specific case.

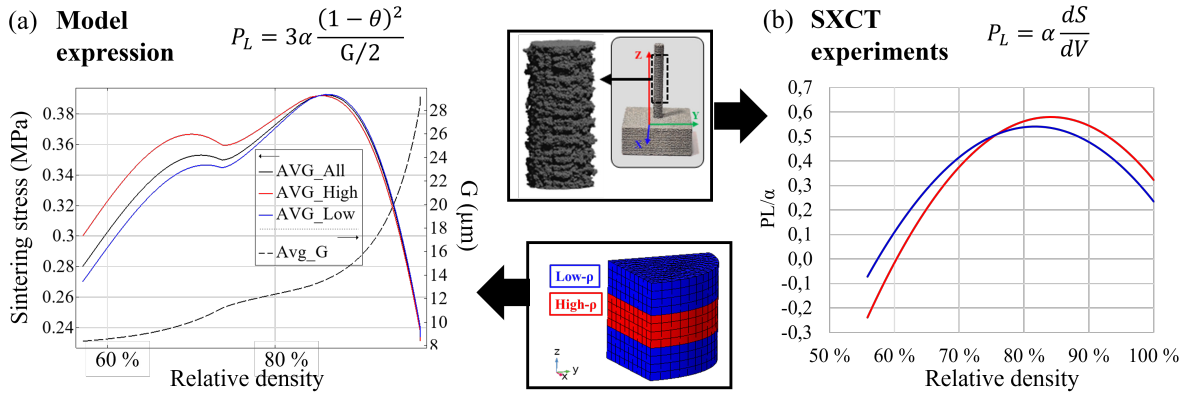

Figure 28. (a) Effective sintering stress calculated within the FEM simulation. (b) Sintering stress derived from the SXCT characterization of pore volume and surface area. Redrawn from [44].

6.4 FEM calculation of sintering of BJT components

Continuum mechanics sintering models present a powerful tool for simulating the BJT sintering process at the macro-scale. Implemented within finite element analysis (FEA) software, these models can predict the geometrical evolution during sintering, including the evolution of microstructural details like relative density and grain size. To validate the approach used, the model was implemented and solved by Finite

Element Method (FEM) using COMSOL Multiphysics® simulation software. The following sintering model parameters were employed within the simulation results summarized on each section:

- Normalized bulk viscosity (ψ): Equation (12) was used throughout all studies. However, in section 6.4.3, additional comparisons were made with alternative ψ expressions from equations (6) and (13).
- Normalized shear viscosity (φ): Equation (4).
- Sintering stress (P_L): Equation (18), including the grain kinetic equation (8).
- Powder material shear viscosity (η_0): equation (16) was used on modelling in section 6.4.2 and 6.4.3, equation (17) was used for the modelling results in section 6.4.1.

The inelastic behavior of materials is often described by the rate of the inelastic quantity, especially if the behavior is time dependent and nonlinear [118]. Therefore, the simulation of sintering was approached by introducing an inelastic contribution to the material strain rate [119,120]:

$$\dot{\boldsymbol{\varepsilon}}_{ij}^{in} = \frac{\boldsymbol{\sigma}'_{ij}}{2\eta_0\varphi} + \frac{\sigma_{kk} - P_L}{18\eta_0\psi}\delta_{ij} \qquad (19)$$

Then, the relative density (ρ) and grain size (G) during sintering were implemented as internal variables. Then, its evolution is calculated by solving the corresponding differential equations defined by the mass conservation from equation (9) and the grain growth kinetics from equation (8). Finally, the spatial domain of the components is discretized by the software meshing tool using tetrahedral elements.

The following sections show different studies on the modelling of sintering of BJT parts showcasing various features. The results were compared against experimental data for validation and discussed regarding the observed deformations during sintering and model performance.

6.4.1 Model validation by demonstrator overhang geometries and experimental comparison.

In this section, the model was implemented using the material shear viscosity inspired on the "rule of mixtures" and Reuss model (detailed in section 6.3.2) [116,117]. The normalized bulk viscosity is taken from equation (12) and material constants used are detailed in Table 6. Demonstrator geometries were designed to challenge the extent of shape deformation on different overhang features under gravity.

Figure 29 visually compares the two distinct geometries studied: a "tree geometry" with straight overhangs of varying lengths and thickness, and an "angled beams

geometry" featuring overhangs at diverse angles and lengths. The figure showcases the green BJT parts, the sintered parts, and the subsequent characterization results for each set of geometries. The green relative density measured on the green parts varies between 54% to 56%, while the sintered parts reach up to 98 to 99%. The sintering process clearly altered the shape of the components, especially noticeable in the 2 mm "tree" geometry. The shape deformations arise from gravitational forces pulling on the parts during sintering. As expected, beams with lower angles relative to the horizontal axis and longer lengths suffered the most significant distortions. Furthermore, the BJT green parts shrunk during sintering due to the high densification occurring within the material. This densification resulted in a microstructure characterized by small, isolated pores distributed relatively evenly throughout the sintered components. Additionally, the presence of the delta-ferrite phase was also detected in the sintered materials.

(a) Tree component (2mm thickness)

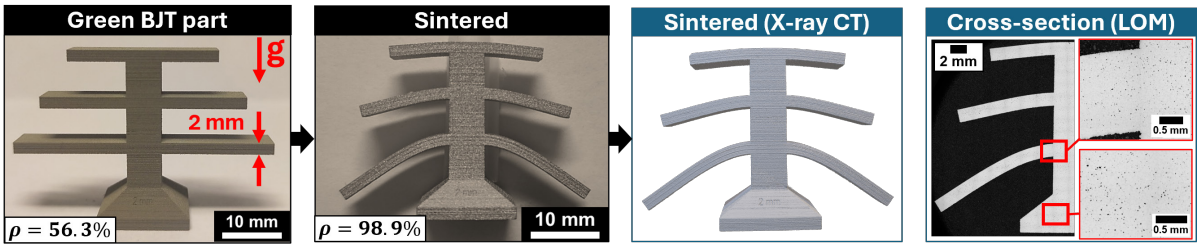

(b) Angled beam component (13 mm length – 15°, 45°, 75°)

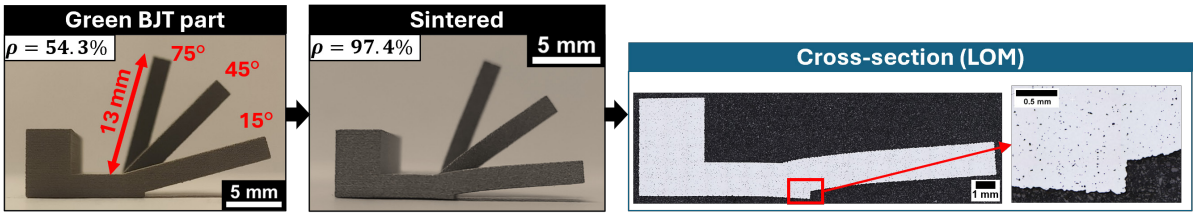

Figure 29. (a) Investigation steps for (a) tree BJT components (printed part, sintered part, X-Ray CT, and LOM images), and (b) angled beam components (printed part, sintered part, and LOM images)

Three different simulations were conducted for each tree geometry, each one using a different normalized bulk viscosity expression (ψ) within the model. Equation (5) was used on the ψ model, equation (13) on the ψ_2 model and equation (12) on the ROH model. Afterwards, the final simulation results of the tree components were compared with the 3D mesh data obtained from the X-Ray Computed Tomography (XCT) characterization. Figure 30 (a) shows the comparison between the three model's results during the sintering simulation. ψ_2 and ROH models show similar density evolution, since these normalized bulk viscosities shows similar ability to adapt to the experimental data by its material constants (see Figure 25). However, a significant difference arises in terms of predicted shape distortions, particularly during the

1370°C dwell step. This is probably caused by the influence of the material shear viscosity η_0 at that temperature. The third model shows even larger distortions during the simulation, collapsing due to the very low material viscosity derived during the material parameters identification process.

Figure 30 (b-d) and (e-g) compare the simulations with XCT data for the 2mm and 3mm tree geometries, respectively. This quantitative analysis reveals the dimensional deviations of each model's solution. Overall, the ROH model outperformed in predicting the final geometry of the sintered components, achieving a maximum deviation of only 0.56 mm and 0.55 mm for the 2 mm and 3 mm trees, respectively. Note that both comparison in Figure 30 (c) and (f) exhibited the largest deviations at the top surface. This suggests that the isotropic assumption of the model might be the main contributing factor for this deviation. Indeed, the dilatometry experiments results shown in Figure 17 revealed slightly larger shrinkages along the building direction (Z axis) for samples printed using the same BJT system and 316L powder.

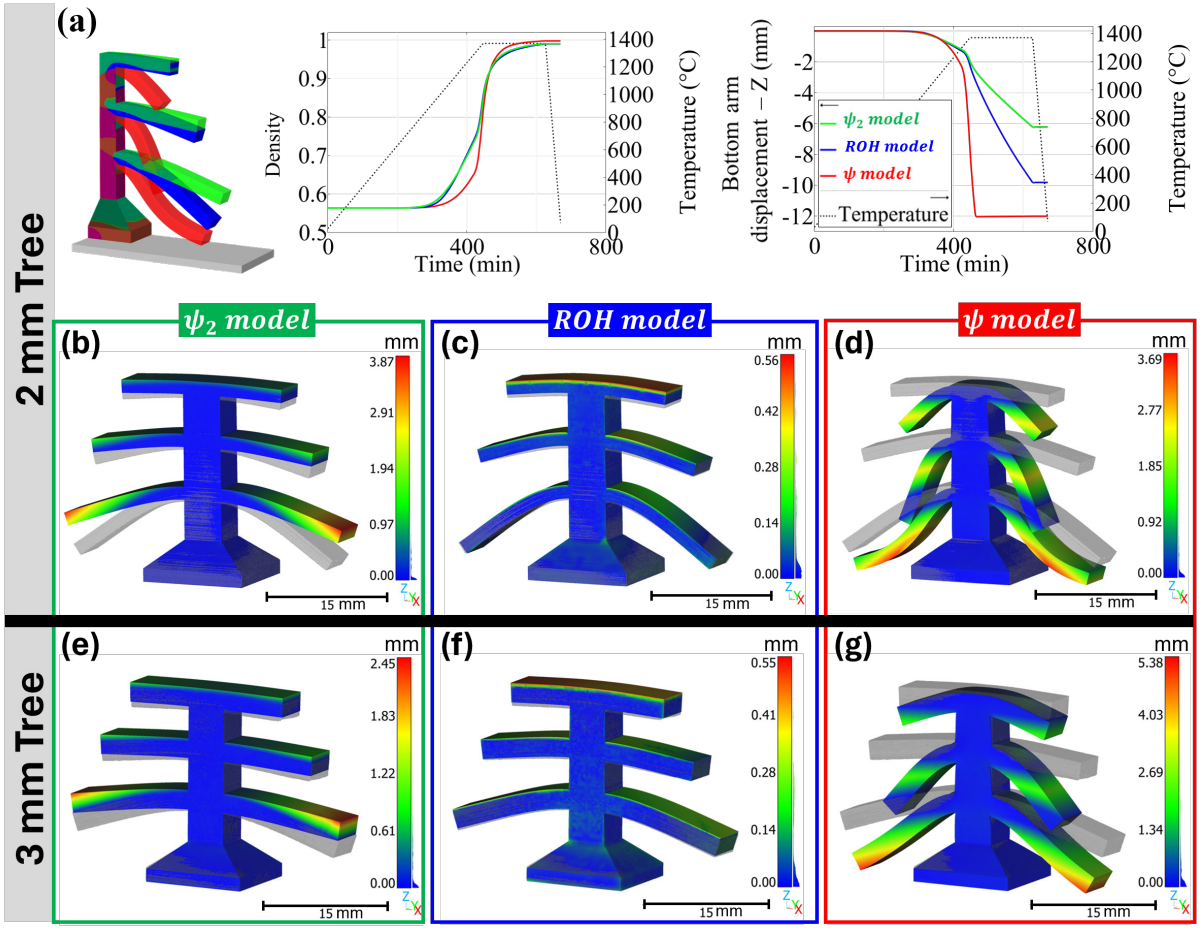

Figure 30. (a) Sintering simulation results for the 3 mm tree geometry. Comparison between the sintered trees experimental XCT characterization and the final simulation results from different models: (b-d) 2 mm tree geometry and (e-g) 3 mm tree geometry.

The simulation conditions of the angled beams geometries were modified to include the effect of contact between the supporting plate and the component during sintering. Since the friction forces are unknow and the sample's weight is relatively small, the frictional forces were assumed negligible during the simulation. Despite the low extent of the surface vertical displacement (~63µm), it was clearly observed within the LOM cross-section image analysis. The simulation results shown in Figure 31 reveals the accurate prediction of the bending behavior of the bottom surface by implementing the contact boundary conditions. Figure 31 (b) overlays cross-section images, revealing the sintered shape and pore characteristics, with a transparent view of the simulated density distribution. While the simulation predicts higher density in compressed areas and lower density in tensioned areas during sintering (~0.1% difference), this variation is too small to be discernable in the LOM cross-sections. Interestingly, the cross-section images seem to show a slightly higher concentration of larger pores in areas under tension, although the difference is subtle. Moreover, the simulation accurately predicts the shape deformations of the beams, particularly for the one with the most significant distortion (15° beam). For the other beams, the model slightly underestimates the actual shape deviation.

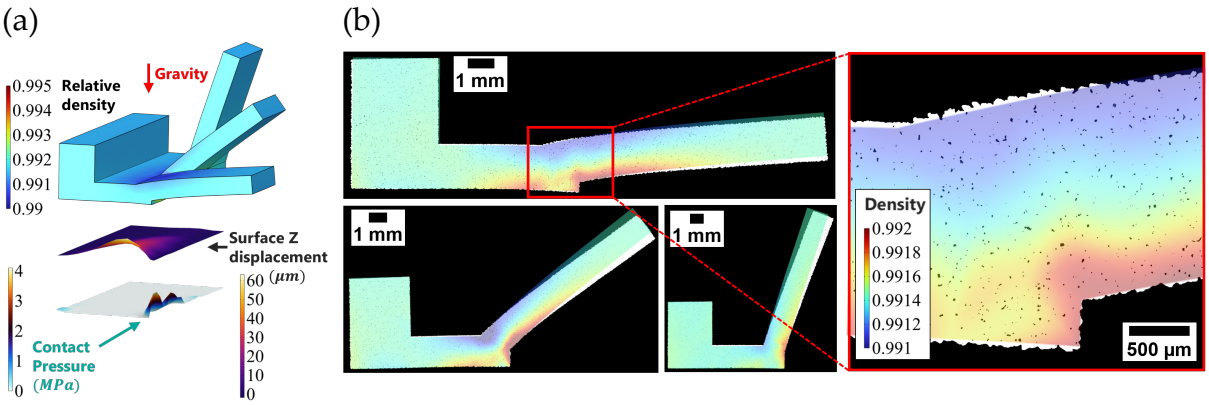

Figure 31. (a) Sintering simulation of the angled beam component incorporating the contact physics. (b) Comparison of LOM cross-section images with the corresponding virtual cross-section of the sintering simulation results of the 13 mm at 15°, 45° and 75° angled beams.

6.4.2 Sintering of BJT demonstrator components: pipe tee connectors

The manufacturing of some engineering parts is highly challenging for BJT due to the potential of high distortions occurring during the sintering process. Tubular shapes, which are inherently unsupported hollowed structures, are one of these examples, especially when low thickness is required. Figure 32 shows the qualitative comparison between sintered pipe tee components and the corresponding simulation results. Due to the small thickness/diameter ratio, G1 and G2 components show the largest deformation after the sintering process, while G3 retains the cylindrical shape of the pipes. The slumping deformation of the horizontal cylinder can be attributed to the

effect of gravity. Also, G1 shows large shape deformations in the vertical cylinder too. This shape deformation may be related to the impact of tension stresses on the vertical cylinder along the XZ plane caused by the slumping of the horizontal pipe. In general, the measured and simulated ratio of axis dimensions (horizontal/vertical axis dimension) of the different pipes revealed similar trends on the final sintered shape deformation. However, larger shape distortions were measured systematically on the sintered geometries.

Figure 32 (d) shows that experimental measured shrinkages and simulations are similar for the geometry with the least shape distortions (G3), whit a maximum difference of 1%. G1 and G2 show larger LZ and lower LY shrinkages, which may be related to the slumping caused by gravity and the restricted shrinkage from frictional forces. However, the simulation results show lower LZ and larger LY shrinkages compared to the sintered parts. This may be related to the overestimation of material viscosity and with the absence of frictional forces on the simulation.

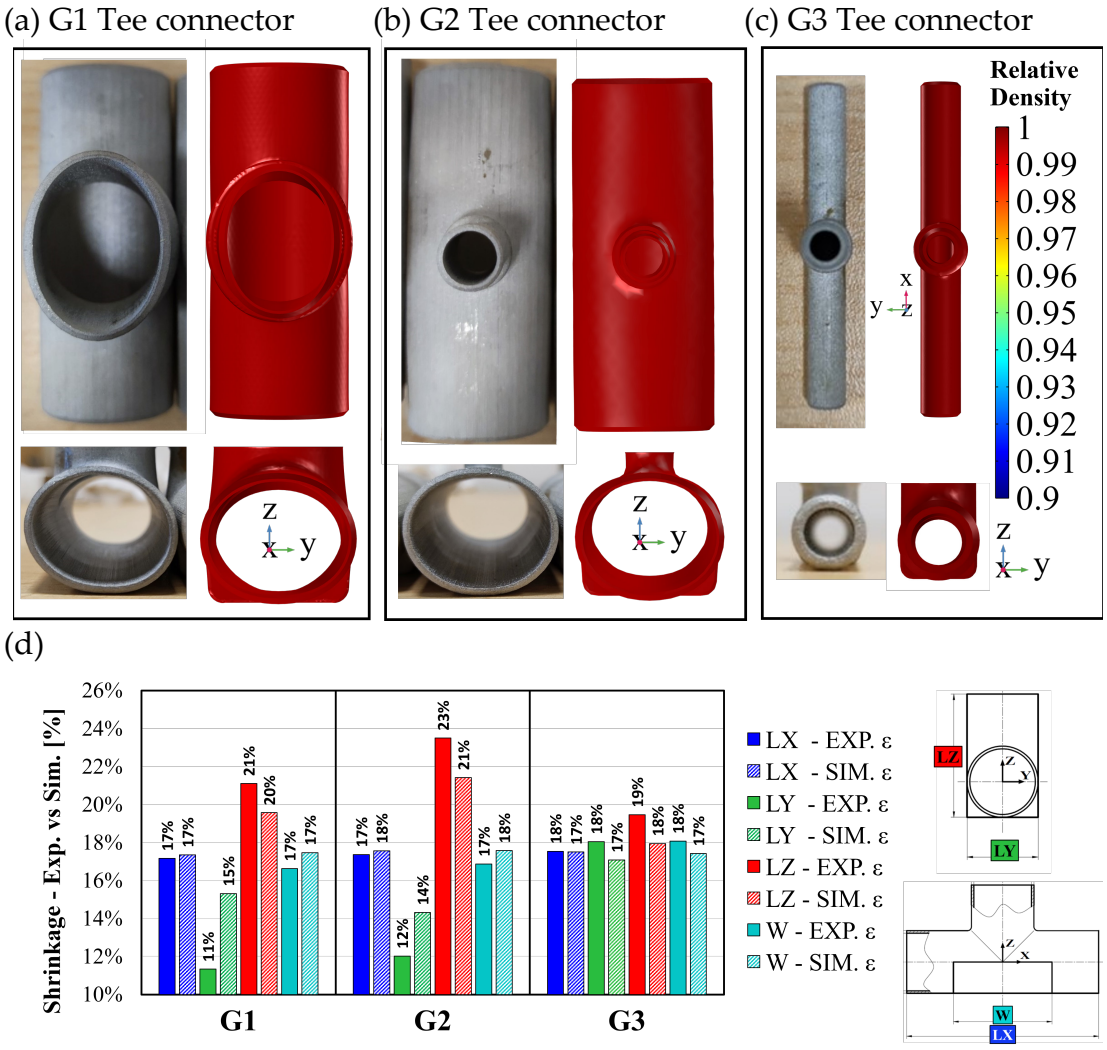

Figure 32. Sintered component and 3D plot of the simulation result for the tee connector geometries: (a) G1, (b) G2, (c) G3. (d) Sintering shrinkages from experiment and simulations.

The simulation of these different components serves to showcase the application of the model to simulation of real engineering BJT components. The detailed comparison with the CMM measurements of the pipe tees distortions revealed that all absolute deviations are below ~1 mm. The simulation seems to overestimate the material viscosity due to the lower deformations and shrinkages observed. However, further optimization of the model material constants can potentially improve the performance of the model.

6.4.3 Prediction of density fluctuations along the building direction

In this section, the phenomenological model developed was implemented using the fluctuation density $\rho_z = f(z)$ from the SXCT green sample (see section 6.2) as initial condition for the relative density variable. This "virtual experiment" simulation results were compared against the experimental SXCT density fluctuation evolution as shown in Figure 33. The density fluctuations are well predicted by the sintering simulation. Small deviations observed in the 1370 °C / 2 min and 60 min profiles may be related to higher densification on the tiny pin geometries used for this study. The fluctuation evolution was characterized by the standard deviation (SD), which shows a slight increase during the heating step, followed by a substantial decrease down to SD~0.5% at the end of the sintering. The simulation and experiments reveal the sintering densification process, which leads to the final homogenization of the density fluctuation induced by the layer-by-layer BJT printing process.

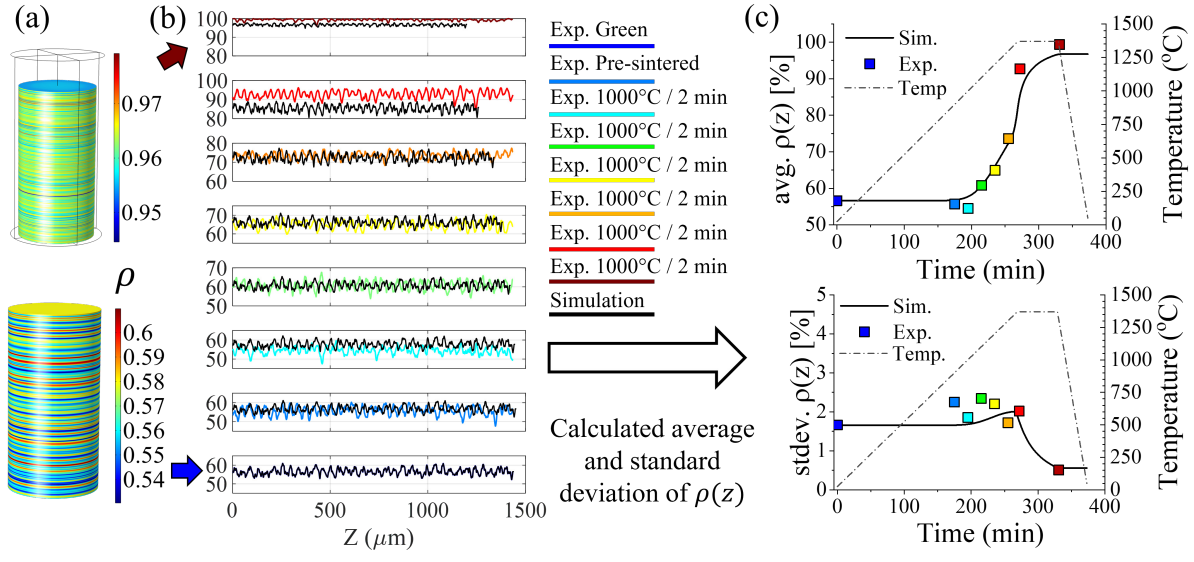

Figure 33. Simulation of the SXCT experiment: (a) 3D plot of the simulated geometry, (b) comparison between simulated and experimental density fluctuation, (c) average and standard deviation of density ρ_z fluctuations [44].

Previous studies suggest that the evolution of densification is highly dependent on the particle size distribution and density heterogeneities, as well as the sintering conditions [77,121–123]. In BJT manufacturing, the use of bi-modal powders or non-optimized printing parameters may lead to severe particle segregation or very large pores within the powder bed [21,35,38,121]. Figure 34 (a) shows the simulation conditions of an idealized symmetrical representative volume with different relative position of initial density $\rho(z)$ (49 - 61%) and grain size $G(z)$ (1 - 130µm). Figure 34 (b) shows the evolution of the density fluctuation of each simulation case, revealing a large increase on the fluctuation for the case 1 and 3 followed by its decrease during the isothermal step. This is related to the initially largest density matching the lowest grain size region, therefore sintering kinetics being faster within this area and leading to an increase between the max/min density. The third case characterizes the opposite behavior, where the low-density region has larger densification kinetics, thus decreasing the initial density fluctuation from the onset of sintering. However, it could be expected that longer sintering times would increase the homogenization of the density. Nevertheless, the simulations reveal the influence of initial heterogeneities of the sintering behavior of BJT parts, which could lead to undesirable effects during sintering. Therefore, the optimization of the initial BJT microstructure could help to mitigate this effect and improve the densification behavior and final properties of the BJT parts.

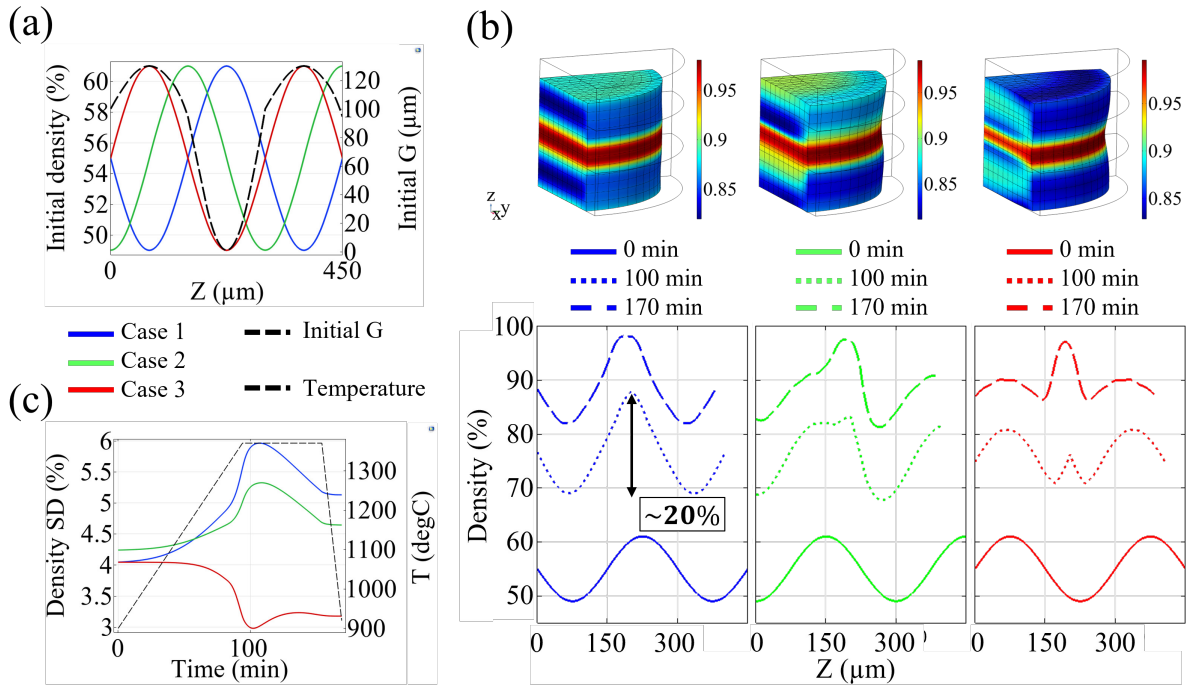

Figure 34. Simulation results for each particle size and density fluctuation case: (a) initial conditions, (b) ρ(z) at several sintering times, (c) evolution of the standard deviation of ρ(z) [44].

CHAPTER 7: CONCLUSIONS

RQ1: What is the impact of different characteristics of the green BJT components and sintering process on dimensional evolution during the sintering process?

- A methodology to characterize densification shrinkages during sintering of BJT parts was established, involving cubical samples for dilatometry experiments along each different axis and data analysis.
- Dilatometry experiments, including in-situ debinding, revealed minimal shrinkages (< 0.5 %) during debinding without significant anisotropy.
- Dilatometry experiments along the different printing axes revealed consistent larger shrinkages along the building direction (Z axis).
- The development of anisotropy is dependent on the BJT printer and powder used for the printing of samples, and its evolution is connected to the densification progress during sintering.
- An increase in the shrinkage rate was observed above ~1310 °C during the heating step of sintering, related to the formation of delta-ferrite.

RQ2: How the microstructural evolution during sintering affects the sintering behavior of BJT stainless steel components?

The microstructural evolution of BJT parts is directly connected to the macroscopic behavior of the parts during the sintering process. Some of the main conclusions obtained can be summarized as follows:

- The pore structure of BJT parts exhibits a "layered" structure with density fluctuations along the building direction. These fluctuations showed a regular pattern with a periodicity matching the printing layer thickness of 42 μm.
- The annihilation of the porosity heterogeneities seems to contribute to the progress of anisotropic shrinkages, particularly along the building direction.
- Microscopy analysis reveals the qualitative differences on the pre-sintered particle's arrangement depending on the BJT printer and powder used, which could be connected to the dissimilar shrinkage behavior observed during the dilatometry experiments.
- The formation of δ-ferrite phase was revealed by EBSD of samples sintered at 1370°C. This suggests that this phase transformation is related to the boosted densification observed by the dilatometry experiments.

- The sintering behavior of the DM 316L powder is analogous to BJT samples. A shift was observed on the boosted shrinkage rate onset temperature, which may be related to the absence of binder affecting the δ-ferrite transformation.
- The grain growth was characterized and measured by image analysis. The pinning effect of the pores was modeled by a kinetic equation involving the density evolution.

RQ3: What are the main material parameters required for a comprehensive sintering model, and how can they be identified experimentally for binder jetted stainless steel?

- Different normalized bulk modulus expressions ψ were studied, this parameter is key for modelling the influence of the pore structure particularities of BJT green components on the densification behavior.
- The expression $\psi = \frac{2}{3}\frac{(1-\theta)^A}{\theta^B}$ shows the best performance. A and B are constants that can adapt the low- and high-porosity dependence of ψ, potentially related to the BJT printing process and powder particle's characteristics.
- The importance of using the right experimental data collection was revealed. Sintering experiments at 4 different temperatures of 1000°C, 1100°C, 1200°C and 1300°C for long times (10 h) were selected to cover a wide combination of θ and T values. To find the surface $\frac{d\theta}{dt}G = f(T,\theta)$ describing the sintering behavior, a single experiment does not provide a single solution, thus leading to inaccurate prediction when simulating a different sintering treatment.
- A new shear viscosity expression η_0 was proposed to include the effect of the δ-ferrite phase transformation during sintering. Initially, a piecewise function was proposed which reveals accurate predictions. Afterward, a new η_0 expression was proposed to include explicitly the fraction evolution of each phase (f_γ, f_δ) as a function of the temperature.
- The model sintering stress evolution during sintering included the grain size evolution, which produces the quadratic evolution with porosity observed. This behavior is similar to the calculated sintering stress from the 3D porous evolution characterized by SXCT.

RQ4: What is the impact of model parameters and BJT geometries on dimensional accuracy and applicability of the developed phenomenological sintering model?

- The implementation of various normalized bulk viscosity expressions revealed its large influence on the simulated shape distortions. This effect is attributed to the differences on the derived material shear viscosity η_0, specially at the highest sintering temperature which also involves long dwell times.

- The distribution of compression/tension stresses within the components induces minor density variations (~0.1%) in the simulation. Regions under tensile stress exhibit decreased densification, whereas compressed regions show increased densification. When simulating the angled beam geometries, the simulation of contact physics between the support plate and the component can improve the accuracy of the predictions. However, the frictional forces may become relevant for large parts.
- The assumption of isotropy leads to error in the predicted densification shrinkages. The tree components revealed ~0.56 mm error on the top surface related to larger shrinkages along the building direction on the sintered parts.

CHAPTER 8: FUTURE SCOPE

While the presented thesis has offered significant contributions, several areas remain open for further exploration. This chapter outlines potential future research directions that could build upon the foundation of this work and unlock new ways for understanding and modelling the sintering behavior of BJT components.

Experimental characterization of BJT sintering:

- Conduct a systematic set of experiments focused on using one BJT printer and several powder variations with different particle size distribution to uncover its relationship with the shrinkage's anisotropy and density evolution during sintering.
- Conduct the same study but varying the printing parameters.
- Perform sintering experiments with in-situ observation and capability for recording the geometrical evolution to enable real-time, accurate measurement of the deformation.
- Quantify the impact of friction between the alumina baseplate and BJT components on shape distortion during sintering, as influenced by both component weight and contact surface area.
- Study the potential influence of part size on the shrinkage's evolution of BJT components.
- Apply the developed methodology for the characterization of sintering behavior using BJT samples produced with other alloys (e.g. copper, 17-4 PH, etc.).

Sintering model development:

- Investigate the effect of printing parameters on the calculation of normalized bulk viscosity constants (A, B) by employing the methodology developed to find possible correlations between them.
- Investigate the influence of BJT green properties on the normalized shear modulus φ to fully understand the simulation of component's shape distortions under diverse sintering conditions, including varying heating rates and dwell temperatures.
- Development and implementation of anisotropy on the sintering model, including a methodology for the identification of anisotropic model parameters.

- Verify the material shear viscosity expression proposed by studying the sintering behavior of variations on the stainless steel alloy composition.

Application and validation of sintering simulations:

- Study of the influence of the frictional forces during the sintering simulations, including the experimental validation and identification of the frictional constants.
- Modelling the in-situ behavior of overhang components and comparing with in-situ characterization of sintering shape deformations to validate the model behavior.
- Develop a compensation method to automatically deform the original geometry. Then, implement an iterative method to find the best compensated geometry by running simulation and compensation iteratively.
- Study the influence of the component size on the temperature distribution within the BJT components during the sintering in an industrial furnace.

ACKNOWLEDGMENTS

First, I want to sincerely thank my supervisors Prof. Eduard Hryha and Prof. Eugene Olevsky for their guidance, insightful advice, and constant encouragement during the last years. Thank you for providing me with the opportunity to carry out this research at Chalmers University and San Diego State University through such a fulfilling and challenging experience. I would also like to express my gratitude to my examiner Prof. Lars Nyborg and all the professors at the industrial and material science department who, at various times, have contributed to enriching this experience both personally and professionally.

I would like to acknowledge the industrial partners Höganäs AB, Digital Metal AB and Sandvik AB, and CAM^2 for the conception and funding of this project. Special thanks to Mats Persson and Linus Lidman for the insights and contributions during our meetings, and the team at Digital Metal and Höganäs for providing me with BJT samples and components that made this work possible. Also, thanks to the team at Sandvik Additive Manufacturing for their contribution during the beginning of this thesis. I would also like to express my gratitude to Dr. Tatiana Mishurova and Dr. Laura Cordova for their invaluable contributions during the sintering and synchrotron characterization experiments.

Thanks to all my PhD colleagues and friends at Chalmers for creating such a great working environment, making it feel like a family during these last years. Special thanks to Bala, Marcos, Erika, Zhuoer and Jaime for the fun times but also for the challenging moments we went through together. I am also grateful for all the support from the research engineers and administrative staff, for always being there to help and make things happen in our department.

I would like to thank all the PTL members for the rewarding time at SDSU and all the inspiring lab meetings we had together. I am deeply grateful for the warm welcome and the great people I met during my time in San Diego. It was an incredibly enriching experience, largely thanks to them. Thanks to Woody, Maricruz, Donald, Ricky, Pau, Charles and many others that shared this experience. Thanks to my soulmate Ivette, for your unwavering support and love during the good and the hard times.

My deepest gratitude to all my family, especially to my parents and sisters, whose love and support are with me in whatever I pursue. Thanks for bringing this family together and all your efforts to overcome the gap between us during this time. Also to all my dear friends in Spain, your constant support, and the feeling of home upon returning are invaluable.

REFERENCES

[1] ASTM International, ISO/ASTM52900-21 Standard Terminology for Additive Manufacturing – General Principles – Terminology, West Conshohocken, PA; ASTM International (2021). http://www.ciri.org.nz/nzrma/technologies.html.

[2] M. Li, W. Du, A. Elwany, Z. Pei, C. Ma, Metal binder jetting additive manufacturing: A literature review, Journal of Manufacturing Science and Engineering, Transactions of the ASME 142 (2020) 1–17. https://doi.org/10.1115/1.4047430.

[3] S.A.M. Tofail, E.P. Koumoulos, A. Bandyopadhyay, S. Bose, L. O'Donoghue, C. Charitidis, Additive manufacturing: scientific and technological challenges, market uptake and opportunities, Materials Today 21 (2018) 22–37. https://doi.org/10.1016/j.mattod.2017.07.001.

[4] A. Lores, N. Azurmendi, I. Agote, E. Zuza, A review on recent developments in binder jetting metal additive manufacturing: materials and process characteristics, Powder Metallurgy 62 (2019) 267–296. https://doi.org/10.1080/00325899.2019.1669299.

[5] A. Popovich, V. Sufiiarov, Metal Powder Additive Manufacturing, New Trends in 3D Printing (2016). https://doi.org/10.5772/63337.

[6] A. Mostafaei, E.L. Stevens, J.J. Ference, D.E. Schmidt, M. Chmielus, Binder jetting of a complex-shaped metal partial denture framework, Addit Manuf 21 (2018) 63–68. https://doi.org/10.1016/j.addma.2018.02.014.

[7] A. Mostafaei, A.M. Elliott, J.E. Barnes, F. Li, W. Tan, C.L. Cramer, P. Nandwana, M. Chmielus, Binder jet 3D printing—Process parameters, materials, properties, modeling, and challenges, Prog Mater Sci 119 (2021) 100707. https://doi.org/10.1016/j.pmatsci.2020.100707.

[8] J. Song, J.C. Gelin, T. Barrière, B. Liu, Experiments and numerical modelling of solid state sintering for 316L stainless steel components, J Mater Process Technol 177 (2006) 352–355. https://doi.org/10.1016/j.jmatprotec.2006.04.111.

[9] D.E.L.U.D.E. Franche-comté, Experiments, modelling and numerical simulation of the sintering process for metallic or ceramic powders, Thesis (2007).

[10] E.A. Olevsky, C. Garcia-Cardona, W.L. Bradbury, C.D. Haines, D.G. Martin, D. Kapoor, Fundamental aspects of spark plasma sintering: II. Finite element analysis of scalability, Journal of the American Ceramic Society 95 (2012) 2414–2422. https://doi.org/10.1111/j.1551-2916.2012.05096.x.

[11] C. Manière, T. Zahrah, E.A. Olevsky, Fluid dynamics thermo-mechanical simulation of sintering: Uniformity of temperature and density distributions, Appl Therm Eng 123 (2017) 603–613. https://doi.org/10.1016/j.applthermaleng.2017.05.116.

[12] R.M. German, Computer modeling of sintering processes, International Journal of Powder Metallurgy (Princeton, New Jersey) 38 (2002) 48–66.

[13] K. Mori, Finite element simulation of powder forming and sintering, Comput Methods Appl Mech Eng 195 (2006) 6737–6749. https://doi.org/10.1016/j.cma.2005.10.015.

[14] C. Manière, L. Durand, A. Weibel, C. Estournès, Spark-plasma-sintering and finite element method: From the identification of the sintering parameters of a submicronic α-alumina powder to the development of complex shapes, Acta Mater 102 (2016) 169–175. https://doi.org/10.1016/j.actamat.2015.09.003.

[15] C. Manière, E.A. Olevsky, Porosity dependence of powder compaction constitutive parameters: Determination based on spark plasma sintering tests, Scr Mater 141 (2017) 62–66. https://doi.org/10.1016/j.scriptamat.2017.07.026.

[16] A. Van der Laan, R. Epherre, G. Chevallier, Y. Beynet, A. Weibel, C. Estournès, Fully coupled electrothermal and mechanical simulation of the production of complex shapes by spark plasma sintering, J Eur Ceram Soc 41 (2021) 4252–4263. https://doi.org/10.1016/j.jeurceramsoc.2021.02.010.

[17] J. Song, T. Barriere, B. Liu, J.C. Gelin, G. Michel, Experimental and numerical analysis on sintering behaviours of injection moulded components in 316L stainless steel powder, Powder Metallurgy 53 (2010) 295–304. https://doi.org/10.1179/003258908X334212.

[18] C. Manière, L. Durand, A. Weibel, C. Estournès, A predictive model to reflect the final stage of spark plasma sintering of submicronic α-alumina, Ceram Int 42 (2016) 9274–9277. https://doi.org/10.1016/j.ceramint.2016.02.048.

[19] C. Manière, C. Harnois, S. Marinel, Porous stage assessment of pressure assisted sintering modeling parameters: a ceramic identification method insensitive to final stage grain growth disturbance, Acta Mater 211 (2021) 116899. https://doi.org/10.1016/j.actamat.2021.116899.

[20] M. Sahli, A. Lebied, J.C. Gelin, T. Barrière, B. Necib, Numerical simulation and experimental analysis of solid-state sintering response of 316 L stainless steel micro-parts manufactured by metal injection molding, International Journal of Advanced Manufacturing Technology 79 (2015) 2079–2092. https://doi.org/10.1007/s00170-015-6983-8.

[21] Y. Lee, P. Nandwana, S. Simunovic, Powder spreading, densification, and part deformation in binder jetting additive manufacturing, Progress in Additive Manufacturing (2021). https://doi.org/10.1007/s40964-021-00214-1.

[22] E. Wheat, G. Shanbhag, M. Vlasea, The master sinter curve and its application to binder jetting additive manufacturing, Journal of Manufacturing Science and Engineering, Transactions of the ASME 142 (2020) 30–32. https://doi.org/10.1115/1.4047140.

[23] S. Sadeghi Borujeni, A. Shad, K. Abburi Venkata, N. Günther, V. Ploshikhin, Numerical simulation of shrinkage and deformation during sintering in metal binder jetting with experimental validation, Mater Des 216 (2022) 110490. https://doi.org/10.1016/j.matdes.2022.110490.

[24] K. Zhang, W. Zhang, R. Brune, E. Herderick, X. Zhang, J. Cornell, J. Forsmark, Numerical simulation and experimental measurement of pressureless sintering of stainless steel part printed by Binder Jetting Additive Manufacturing, Addit Manuf 47 (2021) 102330. https://doi.org/10.1016/j.addma.2021.102330.

[25] B.J. Paudel, D. Conover, J.K. Lee, A.C. To, A computational framework for modeling distortion during sintering of binder jet printed parts, J Micromech Mol Phys 6 (2021) 95–102. https://doi.org/10.1142/S242491302142008X.

[26] MATLAB version 9.13.0.2126072 (R2022b) Update 3, (2022).

[27] H. Blunk, A. Seibel, Toward a Design Compendium for Metal Binder Jetting, Innovative Product Development by Additive Manufacturing 2021 (2023) 39–48. https://doi.org/10.1007/978-3-031-05918-6_3.

[28] S. Mirzababaei, S. Pasebani, A Review on Binder Jet Additive Manufacturing of 316L Stainless Steel, Journal of Manufacturing and Materials Processing 3 (2019) 82. https://doi.org/10.3390/jmmp3030082.

[29] D.Y. Park, S.W. Lee, S.J. Park, Y.-S. Kwon, I. Otsuka, Effects of Particle Sizes on Sintering Behavior of 316L Stainless Steel Powder, Metallurgical and Materials Transactions A 44 (2013) 1508–1518. https://doi.org/10.1007/s11661-012-1477-x.

[30] W. Du, J. Roa, J. Hong, Y. Liu, Z. Pei, C. Ma, Binder Jetting Additive Manufacturing: Effect of Particle Size Distribution on Density, Journal of Manufacturing Science and Engineering, Transactions of the ASME 143 (2021). https://doi.org/10.1115/1.4050306.

[31] R. Bjørk, V. Tikare, H.L. Frandsen, N. Pryds, The Effect of Particle Size Distributions on the Microstructural Evolution During Sintering, Journal of the American Ceramic Society 96 (2013) 103–110. https://doi.org/10.1111/jace.12100.

[32] Y. Bai, G. Wagner, C.B. Williams, Effect of particle size distribution on powder packing and sintering in binder jetting additive manufacturing of metals, Journal of Manufacturing Science and Engineering, Transactions of the ASME 139 (2017) 1–6. https://doi.org/10.1115/1.4036640.

[33] International ASTM, Standard Terminology of Powder Metallurgy B243 − 22, (2022) 1–10. https://doi.org/10.1520/B0243-22.2.

[34] International ASTM, Standard Test Method for Tap Density of Metal Powders and Compounds B527 − 22, B527 (2015) 15–18. https://doi.org/10.1520/B0527-22.2.

[35] G. Miao, W. Du, Z. Pei, C. Ma, A literature review on powder spreading in additive manufacturing, Addit Manuf 58 (2022) 103029. https://doi.org/10.1016/j.addma.2022.103029.

[36] X. Wei, M. Moghadasi, W. Du, C. Ma, Z. Pei, Experimental investigation on ultrasonic hopper dispensing system in powder bed additive manufacturing, J Manuf Process 71 (2021) 106–112. https://doi.org/10.1016/J.JMAPRO.2021.08.040.

[37] G. Miao, M. Moghadasi, W. Du, Z. Pei, C. Ma, Experimental investigation on the effect of roller traverse and rotation speeds on ceramic binder jetting additive manufacturing, J Manuf Process 79 (2022) 887–894. https://doi.org/10.1016/j.jmapro.2022.05.039.

[38] S. Wu, Y. Yang, Y. Huang, C. Han, J. Chen, Y. Xiao, Y. Li, D. Wang, Study on powder particle behavior in powder spreading with discrete element method and its critical implications for binder jetting additive manufacturing processes, Virtual Phys Prototyp 18 (2023). https://doi.org/10.1080/17452759.2022.2158877.

[39] L.C. Capozzi, A. Sivo, E. Bassini, Powder spreading and spreadability in the additive manufacturing of metallic materials: A critical review, J Mater Process Technol 308 (2022) 117706. https://doi.org/10.1016/j.jmatprotec.2022.117706.

[40] H. Miyanaji, N. Momenzadeh, L. Yang, Effect of printing speed on quality of printed parts in Binder Jetting Process, Addit Manuf 20 (2018) 1–10. https://doi.org/10.1016/j.addma.2017.12.008.

[41] N.D. Parab, J.E. Barnes, C. Zhao, R.W. Cunningham, K. Fezzaa, A.D. Rollett, T. Sun, Real time observation of binder jetting printing process using high-speed X-ray imaging, Sci Rep 9 (2019) 1–10. https://doi.org/10.1038/s41598-019-38862-7.

[42] R.M. Lewis, Powder Binder Interactions in 3D Inkjet Printing, (2014).

[43] M. Li, G. Miao, W. Du, Z. Pei, C. Ma, Difference between powder bed density and green density for a free-flowing powder in binder jetting additive manufacturing, J Manuf Process 84 (2022) 448–456. https://doi.org/10.1016/j.jmapro.2022.10.030.

[44] A. Cabo Rios, T. Mishurova, L. Cordova, M. Persson, G. Bruno, E. Olevsky, E. Hryha, Ex-situ characterization and simulation of density fluctuations evolution during sintering of binder jetted 316L, Mater Des 238 (2024) 112690. https://doi.org/10.1016/j.matdes.2024.112690.

[45] Y. Wu, R.M. German, D. Blaine, B. Marx, C. Schlaefer, Effects of residual carbon content on sintering shrinkage, microstructure and mechanical properties of injection molded 17-4 PH stainless steel, J Mater Sci 37 (2002) 3573–3583. https://doi.org/10.1023/A:1016532418920.

[46] E. Hryha, L. Nyborg, A. Malas, S. Wiberg, S. Berg, Carbon control in PM sintering: Industrial applications and experience, Powder Metallurgy 56 (2013) 5–10. https://doi.org/10.1179/0032589912Z.00000000085.

[47] R.M. German, Supersolidus liquid-phase sintering of prealloyed powders, Metall Mater Trans A Phys Metall Mater Sci 28 (1997) 1553–1567. https://doi.org/10.1007/s11661-997-0217-0.

[48] S.-J.L. Kang, Liquid phase sintering, Woodhead Publishing Limited, 2010. https://doi.org/10.1533/9781845699949.1.110.

[49] R.M. German, P. Suri, S.J. Park, Review: Liquid phase sintering, J Mater Sci 44 (2009) 1–39. https://doi.org/10.1007/s10853-008-3008-0.

[50] P. Nandwana, A.M. Elliott, D. Siddel, A. Merriman, W.H. Peter, S.S. Babu, Powder bed binder jet 3D printing of Inconel 718: Densification, microstructural evolution and challenges☆, Curr Opin Solid State Mater Sci 21 (2017) 207–218. https://doi.org/10.1016/j.cossms.2016.12.002.

[51] A. Mostafaei, E.L. Stevens, E.T. Hughes, S.D. Biery, C. Hilla, M. Chmielus, Powder bed binder jet printed alloy 625: Densification, microstructure and mechanical properties, Mater Des 108 (2016) 126–135. https://doi.org/10.1016/j.matdes.2016.06.067.

[52] M. Yang, M.K. Keshavarz, M. Vlasea, A. Molavi-Kakhki, M. Laher, Supersolidus liquid phase sintering of water-atomized low-alloy steel in binder jetting additive manufacturing, Heliyon 9 (2023) e13882. https://doi.org/10.1016/j.heliyon.2023.e13882.

[53] H. Blunk, A. Seibel, Design guidelines for metal binder jetting, Progress in Additive Manufacturing (2023). https://doi.org/10.1007/s40964-023-00475-y.

[54] Z. Ding, H. Zreiqat, M. Mirkhalaf, Rationally-designed self-shaped ceramics through heterogeneous green body compositions, Mater Horiz 5 (2022) 408–415. https://doi.org/10.1039/D2MH00785A.

[55] T.T. Molla, D.K. Ramachandran, D.W. Ni, V. Esposito, F. Teocoli, E. Olevsky, R. Bjørk, N. Pryds, A. Kaiser, H.L. Frandsen, Modeling constrained sintering of bi-layered tubular structures, J Eur Ceram Soc 35 (2014) 941–950. https://doi.org/10.1016/j.jeurceramsoc.2014.10.010.

[56] D. Giuntini, I.W. Chen, E. Olevsky, Sintering shape distortions controlled by interface roughness in powder composites, Scr Mater 124 (2016) 38–41. https://doi.org/10.1016/j.scriptamat.2016.06.024.

[57] T.T. Molla, H.L. Frandsen, R. Bjørk, D.W. Ni, E. Olevsky, N. Pryds, Modeling kinetics of distortion in porous bi-layered structures, J Eur Ceram Soc 33 (2013) 1297–1305. https://doi.org/10.1016/j.jeurceramsoc.2012.12.019.

[58] J.A. Alvarado-Contreras, E.A. Olevsky, R.M. German, Modeling of gravity-induced shape distortions during sintering of cylindrical specimens, Mech Res Commun 50 (2013) 8–11. https://doi.org/10.1016/j.mechrescom.2013.02.007.

[59] M. Zago, N.F.M. Lecis, M. Vedani, I. Cristofolini, Dimensional and geometrical precision of parts produced by binder jetting process as affected by the anisotropic shrinkage on sintering, Addit Manuf 43 (2021) 102007. https://doi.org/10.1016/j.addma.2021.102007.

[60] M. Zago, M. Perina, I. Cristofolini, Preliminary Design Method Accounting for Shape Distortion in Metal Binder Jetting Parts: A Case Study, Lecture Notes in Mechanical Engineering (2023) 925–936. https://doi.org/10.1007/978-3-031-15928-2_81/TABLES/4.

[61] S. Sadeghi Borujeni, G.S. Saluja, V. Ploshikhin, Compensation of sintering deformation for components manufactured by metal binder jetting using numerical simulations, Rapid Prototyp J (2022). https://doi.org/10.1108/RPJ-06-2022-0181.

[62] R.M. German, Coarsening in sintering: Grain shape distribution, grain size distribution, and grain growth kinetics in solid-pore systems, Critical Reviews in Solid State and Materials Sciences 35 (2010) 263–305. https://doi.org/10.1080/10408436.2010.525197.

[63] H. Riedel, J. Svoboda, A theoretical study of grain growth in porous solids during sintering, Acta Metallurgica Et Materialia 41 (1993) 1929–1936. https://doi.org/10.1016/0956-7151(93)90212-B.

[64] P.A. dePoutiloff, P.K. Samal, Sintering of Stainless Steels, Powder Metallurgy (2015) 433–439. https://doi.org/10.31399/ASM.HB.V07.A0006118.

[65] H.S. Kalish, E.N. Mazza, An Evaluation of Dissociated Ammonia and Hydrogen Atmospheres for Sintering Stainless Steel, JOM 1955 7:2 7 (2017) 304–310. https://doi.org/10.1007/BF03377496.

[66] Y. Wu, D. Blaine, B. Marx, C. Schlaefer, R.M. German, Sintering densification and microstructural evolution of injection molding grade 17-4 PH stainless steel powder, Metall Mater Trans A Phys Metall Mater Sci 33 (2002) 2185–2194. https://doi.org/10.1007/s11661-002-0050-4.

[67] A. Simchi, A. Rota, P. Imgrund, An investigation on the sintering behavior of 316L and 17-4PH stainless steel powders for graded composites, Materials Science and Engineering: A 424 (2006) 282–289. https://doi.org/10.1016/J.MSEA.2006.03.032.

[68] R. Bollina, In situ Evaluation of Supersolidus Liquid Phase Sintering Phenomena of Stainless Steel 316L: Densification and Distortion, (2005).

[69] F. Raether, G. Seifert, H. Ziebold, Simulation of Sintering across Scales, Adv Theory Simul 2 (2019) 1900048. https://doi.org/10.1002/adts.201900048.

[70] R.M. German, The Emergence of Quantitative Sintering Theory from 1945 to 1955, 69 (n.d.). https://doi.org/10.1007/s11837-016-2242-1.

[71] A. Kuzmov, E. Olevsky, A. Maximenko, Multi-scale modeling of viscous sintering, Model Simul Mat Sci Eng 16 (2008) 035002. https://doi.org/10.1088/0965-0393/16/3/035002.

[72] A. Maximenko, A. Kuzmov, E. Grigoryev, E. Olevsky, Direct multi-scale modeling of sintering, Journal of the American Ceramic Society 95 (2012) 2383–2388. https://doi.org/10.1111/j.1551-2916.2012.05083.x.

[73] E.A. Olevsky, V. Tikare, T. Garino, Multi-scale study of sintering: A review, Journal of the American Ceramic Society 89 (2006) 1914–1922. https://doi.org/10.1111/j.1551-2916.2006.01054.x.

[74] J. Pan, Modelling sintering at different length scales, International Materials Reviews 48 (2003) 69–85. https://doi.org/10.1179/095066002225010209.

[75] W. Niu, J. Pan, Computer modelling of sintering: theory and examples, Woodhead Publishing Limited, 2010. https://doi.org/10.1533/9781845699949.1.86.

[76] R.M. German, Future Prospects for Sintering, Sintering: From Empirical Observations to Scientific Principles (2014) 513–526. https://doi.org/10.1016/b978-0-12-401682-8.00016-1.

[77] R.K. Bordia, S.J.L. Kang, E.A. Olevsky, Current understanding and future research directions at the onset of the next century of sintering science and technology, Journal of the American Ceramic Society 100 (2017) 2314–2352. https://doi.org/10.1111/jace.14919.

[78] S.H. Chung, H.S. Company, S.J. Park, R.M. German, H.S. Company, S.J. Park, R.M. German, Modeling and Simulation of Press and Sinter Powder Metallurgy, Metals Process Simulation 22 (2018) 323–334. https://doi.org/10.31399/asm.hb.v22b.a0005502.

[79] K.I. Rybakov, E.A. Olevsky, E. V. Krikun, Microwave sintering: Fundamentals and modeling, Journal of the American Ceramic Society 96 (2013) 1003–1020. https://doi.org/10.1111/jace.12278.

[80] D. Agrawal, Microwave sintering of ceramics, composites and metal powders, Woodhead Publishing Limited, 2010. https://doi.org/10.1533/9781845699949.2.222.

[81] C. Manière, S. Chan, E.A. Olevsky, Microwave sintering of complex shapes: From multiphysics simulation to improvements of process scalability, Journal of the American Ceramic Society 102 (2018) 611–620. https://doi.org/10.1111/jace.15892.

[82] J.K. Mackenzie, R. Shuttleworth, A Phenomenological Theory of Sintering, Proceedings of the Physical Society. Section B 62 (1949) 833–852. https://doi.org/10.1088/0370-1301/62/12/310.

[83] R.K. Bordia, G.W. Scherer, On constrained sintering-I. Constitutive model for a sintering body, Acta Metallurgica 36 (1988) 2393–2397. https://doi.org/10.1016/0001-6160(88)90189-7.

[84] T. Kraft, H. Riedel, Numerical simulation of solid state sintering; model and application, J Eur Ceram Soc 24 (2004) 345–361. https://doi.org/10.1016/S0955-2219(03)00222-X.

[85] Z.Z. Du, A.C.F. Cocks, Constitutive models for the sintering of ceramic components-I. Material models, Acta Metallurgica Et Materialia 40 (1992) 1969–1979. https://doi.org/10.1016/0956-7151(92)90183-F.

[86] C. Van Nguyen, S.K. Sistla, S. Van Kempen, N.A. Giang, A. Bezold, C. Broeckmann, F. Lange, A comparative study of different sintering models for Al2O3, Journal of the Ceramic Society of Japan 124 (2016) 301–312. https://doi.org/10.2109/jcersj2.15257.

[87] H.G. Kim, O. Gillia, D. Bouvard, A phenomenological constitutive model for the sintering of alumina powder, J Eur Ceram Soc 23 (2003) 1675–1685. https://doi.org/10.1016/S0955-2219(02)00411-9.

[88] E.A. Olevsky, Theory of sintering: From discrete to continuum, Materials Science and Engineering R: Reports 23 (1998) 41–100. https://doi.org/10.1016/S0927-796X(98)00009-6.

[89] J. Svoboda, H. Riedel, R. Gaebel, A model for liquid phase sintering, Acta Mater 44 (1996) 3215–3226. https://doi.org/10.1016/1359-6454(95)00440-8.

[90] R.M. German, Computer Models, 2014. https://doi.org/10.1016/b978-0-12-401682-8.00014-8.

[91] J. Besson, M. Abouaf, Rheology of Porous Alumina and Simulation of Hot Isostatic Pressing, Journal of the American Ceramic Society 75 (1992) 2165–2172. https://doi.org/10.1111/j.1151-2916.1992.tb04479.x.

[92] M. Abouaf, J.L. Chenot, G. Raisson, P. Bauduin, Finite element simulation of hot isostatic pressing of metal powders, Int J Numer Methods Eng 25 (1988) 191–212. https://doi.org/10.1002/nme.1620250116.

[93] C.H. Hsueh, A.G. Evans, R.M. Cannon, R.J. Brook, Viscoelastic stresses and sintering damage in heterogeneous powder compacts, Acta Metallurgica 34 (1986) 927–936. https://doi.org/10.1016/0001-6160(86)90066-0.

[94] R.K. Bordia, G.W. Scherer, On constrained sintering-II. Comparison of constitutive models, Acta Metallurgica 36 (1988) 2399–2409. https://doi.org/10.1016/0001-6160(88)90190-3.

[95] V.V. Skorohod, Rheological basis of the theory of sintering, (1972).

[96] M.W. Reiterer, K.G. Ewsuk, J.G. Argüello, An arrhenius-type viscosity function to model sintering using the Skorohod-Olevsky viscous sintering model within a finite-element code, Journal of the American Ceramic Society 89 (2006) 1930–1935. https://doi.org/10.1111/j.1551-2916.2006.01041.x.

[97] C. Manière, S. Chan, G. Lee, J. McKittrick, E.A. Olevsky, Sintering dilatometry based grain growth assessment, Results Phys 10 (2018) 91–93. https://doi.org/10.1016/j.rinp.2018.05.014.

[98] G. Kerbart, C. Manière, C. Harnois, S. Marinel, Predicting final stage sintering grain growth affected by porosity, Appl Mater Today 20 (2020). https://doi.org/10.1016/j.apmt.2020.100759.

[99] J. Schindelin, I. Arganda-Carreras, E. Frise, V. Kaynig, M. Longair, T. Pietzsch, S. Preibisch, C. Rueden, S. Saalfeld, B. Schmid, J.Y. Tinevez, D.J. White, V. Hartenstein, K. Eliceiri, P. Tomancak, A. Cardona, Fiji: An open-source platform for biological-image analysis, Nat Methods 9 (2012) 676–682. https://doi.org/10.1038/nmeth.2019.

[100] ASTM International, ISO/ASTM 52908:2023 - Additive manufacturing of metals — Finished part properties — Post-processing, inspection and testing of parts produced by powder bed fusion, West Conshohocken, PA; ASTM International (2023). https://www.iso.org/standard/81779.html (accessed February 20, 2024).

[101] ASTM International, Standard Test Methods for Density of Compacted or Sintered Powder Metallurgy (PM) Products Using Archimedes' Principle, 2013. https://doi.org/10.1520/B0962-17.2.

[102] P. Lehto, H. Remes, T. Saukkonen, H. Hänninen, J. Romanoff, Influence of grain size distribution on the Hall-Petch relationship of welded structural steel, Materials Science and Engineering A 592 (2014) 28–39. https://doi.org/10.1016/j.msea.2013.10.094.

[103] A. International, Standard Test Methods for Determining Average Grain Size, Astm E112-10 (2010) 1–27. https://doi.org/10.1520/E0112-13.1.4.

[104] A. Cabo Rios, E. Olevsky, E. Hryha, M. Persson, R.K. Bordia, Analytical models for initial and intermediate stages of sintering of additively manufactured stainless steel, Acta Mater 249 (2023) 118822. https://doi.org/10.1016/j.actamat.2023.118822.

[105] A. Cabo Rios, E. Hryha, E. Olevsky, P. Harlin, Sintering anisotropy of binder jetted 316L stainless steel: part I – sintering anisotropy, Powder Metallurgy 65 (2022) 273–282. https://doi.org/10.1080/00325899.2021.2020485.

[106] A. Cabo Rios, E. Hryha, E. Olevsky, P. Harlin, Sintering anisotropy of binder jetted 316L stainless steel: part II – microstructure evolution during sintering, Powder Metallurgy 65 (2022) 283–295. https://doi.org/10.1080/00325899.2021.2020486.

[107] F. Wang, S. You, D. Jiang, X. Yuan, R. Fu, F. Ning, Microstructure evolution, phase formation, corrosion, and mechanical properties of stainless steel fabricated by extrusion-based sintering-assisted additive manufacturing, Addit Manuf 75 (2023) 103746. https://doi.org/10.1016/J.ADDMA.2023.103746.

[108] N. Lecis, M. Mariani, R. Beltrami, L. Emanuelli, R. Casati, M. Vedani, A. Molinari, Effects of process parameters, debinding and sintering on the microstructure of 316L stainless steel produced by binder jetting, Materials Science and Engineering A 828 (2021) 142108. https://doi.org/10.1016/j.msea.2021.142108.

[109] B. Barthel, S.B. Hein, C. Aumund-Kopp, F. Petzoldt, Influence of Particle Size Distribution in Metal Binder Jetting – Effects on the Properties of Green and Sintered Parts, in: Procedia EuroPM 2019: International Powder Metallurgy Congress and Exhibition, 2019.

[110] A. Mostafaei, P. Rodriguez De Vecchis, I. Nettleship, M. Chmielus, Effect of powder size distribution on densification and microstructural evolution of binder-jet 3D-printed alloy 625, Mater Des 162 (2019) 375–383. https://doi.org/10.1016/j.matdes.2018.11.051.

[111] D. Huber, L. Vogel, A. Fischer, The effects of sintering temperature and hold time on densification, mechanical properties and microstructural characteristics of binder jet 3D printed 17-4 PH stainless steel, Addit Manuf 46 (2021) 102114. https://doi.org/10.1016/j.addma.2021.102114.

[112] M. Ziaee, E.M. Tridas, N.B. Crane, Binder-Jet Printing of Fine Stainless Steel Powder with Varied Final Density, JOM 69 (2017) 592–596. https://doi.org/10.1007/s11837-016-2177-6.

[113] K.T. Kim, Y.C. Jeon, Densification behavior and grain growth of tool steel powder under high temperature, Acta Mater 46 (1998) 5745–5754. https://doi.org/10.1016/S1359-6454(98)00261-4.

[114] C.R. Alberto, E.A. Olevsky, E. Hryha, M. Persson, Modelling of δ-ferrite transformation effect on the sintering behaviour of 316L binder jetted components, in: WorldPM 2022, EPMA, Lyon, France, 2022.

[115] K.K. Chawla, Micromechanics of Composites, Composite Materials (1987) 177–203. https://doi.org/10.1007/978-1-4757-3912-1_10.

[116] D. Stefaniuk, M. Kachanov, Voigt-Reuss and Hashin-Shtrikman bounds revisited, Int J Eng Sci 191 (2023) 103903. https://doi.org/10.1016/J.IJENGSCI.2023.103903.

[117] A. Reuss, Berechnung der Fließgrenze von Mischkristallen auf Grund der Plastizitätsbedingung für Einkristalle ., ZAMM - Journal of Applied Mathematics and Mechanics / Zeitschrift Für Angewandte Mathematik Und Mechanik 9 (1929) 49–58. https://doi.org/10.1002/ZAMM.19290090104.

[118] Structural Mechanics Module User's Guide. COMSOL Multiphysics® v. 6.2. COMSOL AB, Stockholm, Sweden. 2023, (n.d.).

[119] J.G. Argüello, M.W. Reiterer, K.G. Ewsuk, Verification, performance, validation, and modifications to the sovs continuum constitutive model in a nonlinear large-deformation finite element code, Journal of the American Ceramic Society 92 (2009) 1442–1449. https://doi.org/10.1111/j.1551-2916.2009.03008.x.

[120] B. Lester, Verification of the Skorohod-Olevsky Viscous Sintering (SOVS) Model, 2017.

[121] E. Wheat, M. Vlasea, J. Hinebaugh, C. Metcalfe, Sinter structure analysis of titanium structures fabricated via binder jetting additive manufacturing, Mater Des 156 (2018) 167–183. https://doi.org/10.1016/j.matdes.2018.06.038.

[122] E. Olevsky, A. Molinari, Instability of sintering of porous bodies, Int J Plast 16 (2000) 1–37. https://doi.org/10.1016/S0749-6419(99)00032-7.

[123] D.J. Green, O. Guillon, J. Rödel, Constrained sintering: A delicate balance of scales, J Eur Ceram Soc 28 (2008) 1451–1466. https://doi.org/10.1016/j.jeurceramsoc.2007.12.012.